Distributed fiber optic strain sensing in deep mixed columns

Sølve Hov,[1] Henrik Meland,[2] Anil Helvacioglu,[3] Robert Thurner,[4] and Åse Marit Wist Amdal[5]

[1]Senior Engineer and PhD candidate, Geotechnics and Natural Hazards, Norwegian Geotechnical Institute and Department of Civil and Environmental Engineering, Norwegian University of Science and Technology, 7034 Trondheim, Norway; email: solve.hov@ngi.no (Corresponding author). ORCID: 0000-0002-1161-5110

[2]Senior Engineer, Field Testing and Offshore Instrumentation, Norwegian Geotechnical Institute, 0484 Oslo; email: henrik.meland@ngi.no

[3]Design & Projects Engineer, Keller Grundläggning AB, 434 39 Kungsbacka, Sweden; email: anil.helvacioglu@keller.com

[4]Regional Manager Subsidiaries SWE / NOR, Keller Grundläggning AB, 434 39 Kungsbacka, Sweden; email: robert.thurner@keller.com

[5]Senior Engineer, Geotechnics and Natural Hazards, Norwegian Geotechnical Institute, 7034 Trondheim, Norway; email: ase.marit.wist.amdal@ngi.no

ABSTRACT

This paper presents a novel case study where distributed fiber optic sensing (DFOS) was successfully employed in wet deep mixed columns for distributed strain sensing (DSS). Sensors were installed in the cement-improved columns and interrogated with optical frequency domain reflectometry using Rayleigh backscattering to obtain a spatial resolution of 2–3 cm. The improved ground was gradually loaded with

an up to 5.5 m thick fill during frequent interrogation of the sensors. The sensors were shown to be highly responsive to loading, and measured strains ranged from around 150 $\mu\varepsilon$ to around 3,900 $\mu\varepsilon$, indicating a considerable vertical column variability resulting in large strain gradients, i.e., change of strain per unit length of sensor. Special attention was given to strain coupling between sensors and improved soil, and a stress equilibrium considerations indicate that the interface shear strength was sufficient to maintain the measured strain gradients. Current design methodologies of strain magnitude and strain rate also agreed well with the measured strains, excluding the effect of a few weakness zones exhibiting large strains. The paper is completed with a discussion around practical issues concerning installation of DFOS sensors in deep mixing applications. In all, it is shown that DFOS is also a highly promising technology in the field of ground improvement by deep mixing and can reveal the performance of an improved ground with unprecedented spatial resolution.

1. INTRODUCTION

Distributed fiber optic sensing (DFOS) is a technology which allows sensing of temperature, strain, and vibrations with high spatial and temporal resolution and can provide valuable information on the performance and behaviour of a geotechnical structure or soil deposits (Bado & Casas, 2021; Hartog, 2017; Kechavarzi et al., 2016; Soga & Luo, 2018). DFOS is, for example, extensively used to investigate the behaviour and response of geotechnical structures such as concrete or steel piles (Monsberger et al., 2020; Pelecanos et al., 2018; Seo, 2020; Sienko et al., 2018; Xu et al., 2018), anchors (W. Chen et al., 2023), secant piled or diaphragm walls (Lin et al., 2023; Mohamad et al., 2011), or soil deformations (J. Liu et al., 2019; Yeskoo & Soga, 2022; Zhang et al., 2018). In the former examples, optical fiber sensors are attached to reinforcement cages of in situ casted piles or grooved into the outer perimeter of pre-

44 casted piles. This enables a detailed investigation of the strain and force behaviour and gives insights
45 into the behaviour of the geotechnical structure.

46 However, DFOS has not yet been applied for deep mixing purposes, which is one of the most used
47 ground improvement techniques to increase the bearing capacity and foundation stiffness in areas with
48 soft soils. The method is performed by mechanically mixing a cementitious binder, creating columnar
49 inclusions of increased strength and stiffness compared to the surrounding natural soil (Kitazume &
50 Terashi, 2013; Larsson, 2005). However, two challenges arise that differ from DFOS applications in other
51 geotechnical structures, e.g., concrete piles. Firstly, there are no structural elements of steel or concrete
52 to which the fiber sensor can be attached, and thus the installation of the fiber sensor in deep mixed
53 columns requires other approaches. Secondly, the considerably lower stiffness of a deep mixed column
54 compared to a concrete pile might result in a high risk of soil-sensor strain decoupling so that the
55 measured strains are not representative of the column strain. Arguably, this has caused the lack of
56 published results of DFOS applications in this civil engineering area, despite the possible advantages of a
57 deeper understanding of the behaviour of deep mixed columns.

58 This paper presents a novel case study where DFOS was successfully employed in deep mixed columns
59 for distributed strain sensing (DSS). A clay was improved with wet deep mixed columns to increase the
60 composite ground stiffness to reduce likely settlements for a future 16-storey building. DSS sensors
61 were installed vertically in columns to obtain continuous strain profiling as the improved ground was
62 loaded with a trial embankment. Conventional geotechnical instrumentation, including pore pressure
63 and settlement measurements, was also performed.

64 The DSS sensors were interrogated using optical backscatter reflectometry of Rayleigh backscattering in
65 favour of Brillouin backscattering which is more commonly used in civil engineering applications. Whilst
66 Brillouin backscattering is suitable for long-range application with spatial resolutions typically in the

range of 0.5-2 m, Rayleigh backscattering is most suitable for shorter-range but with a superior spatial resolution of 1-3 cm or higher. Short-range here implies sensor lengths of up to around 70 m; however, this is within the range of most deep mixing applications where columns depths typically are up to 30 m for onshore applications (Kitazume & Terashi, 2013; Larsson, 2005). The working principle behind Rayleigh backscattering is outlined in later sections of the paper. In addition to presenting results from the instrumentation and sensing, special attention is given to strain coupling between sensor and improved soil as well as practical challenges around sensor installation in deep mixing applications.

2. MATERIALS AND METHODS

2.2 Site conditions

The soil conditions at the site, located in Trondheim, Norway, consisted of 4–5 m of made ground overlying around 50 m deep natural deposit of low-sensitive clay, as illustrated in Figure 1. The clay deposit is fairly uniform with a density of around 2–2.1 t/m^3, a natural water content of around 20–35% and a plasticity index of around 20–35%. The clay has an intact undrained shear strength that starts at approximately 50 kPa at the top and increases at around 3 kPa/m. The remoulded shear strength is 5–10 kPa except for a stiffer layer at around 10 m depth with a remoulded strength of up to 20–30 kPa, i.e., considerably higher than typical soft Nordic clays. Figure 1 shows a cone penetration test (CPT) result performed in the natural clay.

The overconsolidation at the top of the clay layer was around 150 kPa, decreasing to around 40 kPa at 20 m depth. Constant rate of strain oedometer tests showed oedometer moduli (M_{soil}) of around 10,000–20,000 kPa in the overconsolidated (OC) range and 4,000–6,000 kPa in the normally consolidated (NC) range. The coefficient of consolidation (c_v) varied between 10 and 20 m^2/year in the OC range and between 4 to 6 m^2/year in the NC range. The pore pressure conditions were slightly above hydrostatic pressure.

2.2 Construction scheme and testing programme

Before executing the deep mixing works, the 4–5 m thick original made ground was excavated down to the top of the clay, whereby a working platform of 1.5 m was constructed. Deep mixed columns, outlined in detail below, were installed during a five-week period along with installation of DSS sensors and piezometers in the columns. Some of the conventional geotechnical instrumentation equipment was installed 5-10 weeks after column execution, whereafter the excavated pit was backfilled during a seven-week period to a level of +15 and finally up to +16, i.e., around 5.5 m above the working platform at +10.5. The stress increase at the top of the improved ground (q), i.e., due to the weight of the fill, was approximately 105 kPa. Table 1 gives an overview of the construction, installation, and monitoring programme. Figure 1 shows the ground improvement plan view and cross section including locations of DSS sensors and other instrumentation. Measurements, including interrogations of DSS sensors and surveying of settlement plates (SP) are designated 'M1' to 'M10'.

2.3 Deep mixed columns

Deep mixed columns with 1.2 m diameter were installed at 1.5 m centre-to-centre distance in a rectangular pattern, giving an area (and volume) replacement factor of 50%. The effective column lengths were 18.5 m (Figure 1). The mixing was performed using the wet method, notably the first wet mixing project in Norway where dry deep mixing otherwise is used. The wet mixing method was chosen due to the low sensitivity and high remoulded shear strength of the natural clay which would make the mechanical mixing insufficient using a dry binder. The column execution consisted of two mixing cycles, where only water, around 150 litres per meter column, was added to the clay in the first cycle to increase its mixability. The slurry, containing standard Portland cement CEM II 42.5/B-M as binder, was added in the second mixing cycle. The water-cement-ratio of the slurry was 0.8 and the resulting

theoretical dry binder quantity was 200 kg per m^3 of clay. In all, around 293 litres of water were added to the soil through the first and second mixing cycles.

Strength verification of the columns was made based on wet grab samples, i.e., taken from freshly mixed columns, compacted in moulds and left to cure in a temperature-controlled water bath holding 40–45°C. This was done to speed up the soil-binder reactions since the total construction time was rather short at around 1.5 months, and strength verification at an early stage was necessary. By using the maturity concept a curing time of around 4–6 days in 40–45°C is sufficient to simulate around 28 days of curing in 20°C (Bache et al., 2022; Kitazume, 2022). The resulting unconfined compressive strengths (q_u) ranged between ~600 and ~1,100 kPa with an average of ~830 kPa and a coefficient of variation of ~16%. The Youngs' modulus ($E_{50} = E_{50,col}$) was estimated to be around 100 times q_u, i.e., around 80,000 kPa (Hov & Larsson, 2023; Kitazume & Terashi, 2013; Paniagua et al., 2022). Subsequent sample coring was not successful due to sample disturbance which gave unreliable strength estimates.

2.4 Settlement, pore pressure and temperature measurements

Piezometers including thermometer sensors were installed in column J5 immediately after column execution mainly to monitor temperature changes for DSS purposes. The piezometers were installed at depths of 3.5 m, 8.5 m, and 13.5 m as shown in Figure 1. Two piezometers were also installed in the clay at a later stage to monitor pore pressure dissipation within and beneath the improved ground (Figure 1).

Vertical settlements were measured by three conventional settlement plates with base plates positioned at elevation level +9, i.e., at the top of the columns. Risers were attached to the plates and surrounded by a protective plastic casing. The location of the settlement plates is shown in Figure 1.

2.5 Fiber optic sensors

The DSS sensors installed in the deep mixed columns were of the type EpsilonSensor, manufactured by Nerve-Sensors (SHM System Sp). This is a 3 mm diameter braided monolithic sensor consisting of a fiberglass reinforced polyester fiber with epoxide protective coating. The optical fiber is integrated into the epoxide during pultrusion to avoid any layering. The elastic axial modulus is 3 GPa and axial stiffness (EA) is 21 kN. The sensors were terminated with an optical dampening at the end. The total length of the sensors was 50 m with an additional 10 m of pigtail.

The sensors were installed immediately after column execution by placing a 1.5 m plastic casing in the working platform later surrounded by backfill. The sensors were then pushed down through the centre of the casing and into the fresh columns using a geotechnical drilling rig and a sacrificial anchor to which the sensors were attached. The anchors were pushed down carefully with a drilling rod, having the sensors alongside the drilling rod. The drilling rod was then extracted, leaving the anchor and sensor in the ground. It was assumed that the freshly mixed clay collapsed around the sensors to achieve full physical contact. The installation was however unexpectedly challenging due to the high remoulded shear strength and sticky character of the clay, and three sensors broke due to too high resistance during penetration, damaging the optical dampening effect and resulting in too uncertain strain data. Two sensors were however successfully installed to 8.5 m and 10.5 m depth in columns designated L6 and K6, respectively (Figure 1). These sensors slipped from the sacrificial anchors at these depths, but the optical dampening was not damaged. Due to the high penetration resistance, the sensors were naturally pre-tensioned as a result of the installation process. After installation, the sensors were placed into protective plastic tubes from the top of the column to the measurement point (Figure 1). Figure 2 shows photographs of the installation work.

2.6 Interrogation technique

Interrogation of all sensors was performed with the optical backscatter reflectometer OBR4600 from Luna Innovations, see Figure 3(a). This interrogator uses Rayleigh backscattering and optical frequency domain reflectometry (OFDR), and since this is a rather unusual interrogation technique in geotechnical engineering applications, it is briefly outlined in the following sections.

Rayleigh scattering as a physical phenomenon occurs when incident light interacts with particles smaller than the light wavelength and changes direction. The interaction is elastic, meaning that the light does not loose energy, change its wavelength or frequency as it is reflected. This differs from, e.g., Brillouin scattering were the frequency changes and can directly be related to e.g. strain or temperature changes. The Rayleigh scattering occurs due to intrinsic small-scale variations of the refractive index of the silica core, caused by randomly distributed density fluctuations and impurities.

The process is illustrated in Figure 3(b). A tunable laser source emits a light signal with sweeping wavelengths, referred to as swept-wavelength interferometry (SWI). This light is split into a reference path and into the optical fiber which is interrogated. The received (backscattered) signal from the optical fiber is recombined with the reference path light to create an interference pattern in the frequency domain. By Fourier transform this data is converted into the spatial domain whereby the phase and amplitude are obtained as a function of spatial position (z) along the optical fiber. Data in small segments of the fiber, i.e., gauge length Δz, is then processed by an inverse Fourier transform to convert the data back to the frequency domain, giving a spectral (frequency) signature which is random but static for that particular segment of the optical fiber (Chamoin et al., 2022; Ding et al., 2018; Hartog, 2017). If the fiber is forced to strain (either mechanically or thermally), this spectral signature will change. Thus, by comparing a reference reading to a reading where the optical fiber is strained, illustrated as 'M1' in Figure 3(b), a spectral shift ($\Delta \nu$) is obtained.

This spectral shift is empirically calibrated to temperature or strain changes of the fiber core. Strain (ε) is calculated, assuming zero temperature change:

Equation 1: $$\varepsilon = -\frac{\bar{\lambda}}{k_\varepsilon c}\Delta v$$

where $\bar{\lambda}$ is the scanning centre wavelength, c is the speed of light, and k_ε is the strain coefficient. For most silica fibers, k_ε is ~0.78. Given $\bar{\lambda}$ = 1,550 nm, which is used by the OBR4600 since this gives the lowest attenuation and highest signal-to-noise ratio, the conversion between the Δv and strain is given by a factor -6.67 $\mu\varepsilon/GHz$.

The best spectral shift quality and hence the most reliable strain data was obtained using both a gauge length and a gauge spacing of 2–3 cm, meaning data was obtained at 2–3 cm intervals along the sensor. The strain resolution of OFDR is ±1.0 $\mu\varepsilon$; however, since Rayleigh backscatter is affected by both temperature and strain, strain data need to be separated or corrected when interrogating a monolithic sensor. In this case, temperature was monitored separately by piezometers in an adjacent column J5 (Figure 1). The supplied thermal coefficient for the EpsilonSensor relating strain and temperature data was 10.1 $\mu\varepsilon$/°C.

3. RESULTS

3.1 Temperature and pore pressure

Temperature data is shown in Figure 4. Column J5 showed a gradual increase from around 10–15°C at the time of installation to around 18–21°C, caused by the exothermic cement hydration process. The natural ground temperature in this area is around 6°C. The increase from 6°C to around 10–15°C thus occurred within a few hours before the piezometers were installed. After reaching 18–21°C, the column temperature was fairly constant over time caused by the low thermal conductivity of the improved columns and of the natural clay. These long term elevated temperatures in improved ground have also

been observed in previous studies (Bache et al., 2022). The temperature development in the columns also affected the natural clay in-between as well as increased the temperature to around 10°C at 2.5 m below the improved ground due to heat diffusion.

With a maximum ±2°C variation during the DSS interrogations, the uncertainty in the distributed strain data due to thermal effects will be within a negligible 20 $\mu\varepsilon$.

Figure 5 shows pore pressure data. The piezometer in column J5 was installed during execution of the deep mixed columns and is affected by installation of nearby columns in July 2023. Fill earth works started in late August 2023 and continued until middle of October (Table 1 and Figure 4), generating a pore pressure increase between 27 kPa and 40 kPa which thereafter slightly dissipated over time. The additional piezometers (Pz1 and Pz2) were installed in late October, but compared to measurements before construction started, the data shows an excess pore pressure of 20 kPa in the middle of the improved ground, and 55 kPa at 2.5 m below the improved ground in November. This excess pore pressure dissipates over time.

Figure 6 shows settlements, i.e., vertical displacements of the settlement plates, between measurement M3 and M10, i.e., the period where the settlement plates were measured. All plates show a settlement rate of around 5 mm per month disregarding M10 which deviates from the pattern, possibly due to a measurement error.

3.2 Distributed strain sensing in columns

Results from the DSS in the columns are shown in Figures 7(a) and (b) for column L6 and K6, respectively. The accumulated strains exhibit a considerable variability where the strain at the final reading, M10, varies from around 150 $\mu\varepsilon$ at the lowest up to peaks of around 3,900 $\mu\varepsilon$. The strains, both the overall trend and the peaks, decrease with depth. The top ~1 m is affected by lack of, or insufficient, contact between the sensor and the improved column since the protective plastic casing was bent and

inserted 0.2–0.5 m into the top of the columns to avoid sensor damage, resulting in practically zero strain in this interval. It further seems that it requires ~0.5 m to reach the characteristic strain profile shown at larger depths, which is expected due to a minimum length required to obtain full stress transfer from improved column to sensor. The maximum strains are seen at a depth around 1–2 m, indicating that full contact is achieved here. The strain magnitudes at M10 are similar to reported values for casted concrete piles, although with a higher variability (Monsberger et al., 2020; Pelecanos et al., 2018; Seo, 2020; Sienko et al., 2018; Xu et al., 2018).

Figure 8 shows vertical displacements, i.e., integrated strains, versus depth for the two columns. These values are however not fully representative for the full column length since the top around 1 m and bottom 9–10 m is missing. For column K6, the processing of data from measurement M8–M10 showed optical effects that made it difficult to reliably calculate strain below ~6 m depth, and thus the vertical displacements are not shown for M8–M10. Nevertheless, the measured strains show a total compression of 6–8 mm for the top 8–10 m of the columns. The vertical displacement resulting from this compression is shown along with vertical displacement from the settlement plates in Figure 6 for the period between M3 and M10. The difference between these two originates from compression of the lower half of the columns as well as in the underlying clay, with the latter most probably giving the largest displacement due to the transfer of load from the fill through the floating improved ground.

4. DATA ANALYSIS AND DISCUSSION

4.1 Strain coupling sensor – improved column

Studies have shown that the monolithic EpsilonSensor used in this work is internally fully coupled without slippage up to 40,000 $\mu\varepsilon$, i.e., 4% strain (Bednarski et al., 2022; Howiacki et al., 2023; Piątek et al., 2023). There is therefore no need to correct measured strains as for layered sensor systems, and measured strains are considered to be uniform across the whole cross-section of the sensor, so that any

measured strains represent actual mechanically forced strains at its periphery. These forced strains are caused by strains in the improved columns. Moreover, the sensor itself does not act as a reinforcement as the axial stiffness (EA) of the sensor is considerably lower than the columns, around 21 kN compared to around 90,000 kN, respectively.

Whether strain coupling, i.e., full transfer of strains from the improved column to the sensor, is achieved can be assessed by considering stress equilibrium acting on an element of the sensor with element length dz (Ansari & Libo, 1998; Chapeleau & Bassil, 2021; Sun et al., 2019; H. Wang & Dai, 2019), illustrated in Figure 9(a). Stress equilibrium in the positive z-direction assuming a constant shear stress gives:

Equation 2: $$\pi r_c^2 \sigma_c - \pi r_c^2 (\sigma_c + d\sigma_c) + 2\pi r_c \tau_i dz = 0$$

where r_c is the radius of the sensor, σ_c is the sensor stress, τ_i is the mobilised interface shear stress along the sensor, i.e., the interface between sensor and improved soil. Solving for τ_i and combining with Hooke's law ($d\sigma_c = d\varepsilon_c \times E$) yields:

Equation 3: $$\tau_i = \frac{r_c}{2} \frac{d\sigma_c}{dz}$$

Equation 4: $$\tau_i = \frac{r_c}{2} \frac{d\varepsilon_c}{dz} E$$

where ε_c is the sensor strain, E is the Youngs' modulus of the sensor (3 GPa) and $d\varepsilon_c/dz$ is the strain gradient as measured by the sensor, i.e., change in strain with depth. This equation shows the interface shear stress necessary to achieve and maintain the forced strain gradient of the sensor. In other words, any strain gradient in the sensor – resulting in a stress gradient – will need to be in equilibrium with the interface shear stress to avoid slippage. If the interface shear strength, referred to as bond strength, is higher than the interface shear stress, the sensor is able to maintain the strain gradient. Studies show that creep in improved soil is low at stresses below the yield stress (Kitazume & Terashi, 2013; D. Wang

et al., 2015). However, some margin is probably required to avoid creep relaxation at the interface. If a slippage would occur, this would redistribute the strains along the sensor and smoothen the measured strain profile until equilibrium is established, as schematically illustrated in Figure 9(b).

There are no studies of the bond strength for EpsilonSensor embedded in cement-improved clay. However, a study on similarly braided steel rods showed that the bond strength in improved clay was around 0.4 times q_u (C. Chen et al., 2018). Given a q_u of 800 kPa as obtained by the wet grab samples, this would indicate a bond strength of around 300 kPa, a conservative value since this is based on unconfined compression tests with considerably lower effective stresses than present in the in situ improved columns.

The calculated absolute mobilised interface shear stress ($|\tau_i|$) and degree of mobilised bond strength for the last measurement M10 are shown in Figures 10 and 11 for columns L6 and K6, respectively. Naturally, $|\tau_i|$ is proportional to $d\varepsilon_c/dz$. The maximum $|\tau_i|$ is around 150 kPa, reaching up to around 50% of the bond strength at largest $d\varepsilon_c/dz$, although it is mostly below 10–20%. This strongly indicates that the bond strength is sufficient to achieve equilibrium and maintain the $d\varepsilon_c/dz$, thus achieving a full strain coupling.

The strain coupling is further assessed by analysing the experimental data. Figure 12 shows measured strain data extracted from Figure 7 for selected segments of the sensors: between 1.0 m and 2.0 m for column L6 (Figure 12(a)) and between 4.0 m and 5.0 m for column K6 (Figure 12(b)). Figure 12 shows strain data with 2 cm spatial resolution to assess strain transitions around peaks to allow for a visual quality control. The figure clearly shows the gradual and consistent increase of strain for both low and high strain values. Figure 12(a), for example, shows the segment with the highest strain peaks up to 3,500 $\mu\varepsilon$ for column L6 and also the highest strain gradients at around 1.6 m depth. The $|\tau_i|$ is here around 150 kPa, around 50% of the bond strength.

Figures 13(a) and 14(a) show strain over time, i.e., strain rate for measurements M1 to M10 and for depths at 0.2 m intervals for the segments shown in Figure 12. The elevation of the embankment is also shown. Figure 13(b) and 14(b) show strains normalised to the final strain value, and very consistent strain vs. time curves are seen. It shows the highly responsive behaviour of the sensor as the elevation of the fill is increased and the columns are loaded. It also shows similar strain rates for both low and high values of measured strains, indicating that no slippage occurs as illustrated in Figure 9. From around October 2023 the strain development over time is due to consolidation, further analysed below. The final load step to +16 does not affect the sensors, most probably caused by a considerable stress distribution as this layer was smaller (Figure 1(b)).

4.2 Strain magnitude and rate

The strain magnitude and depth trend of the distributed strain data are compared to an analytical design methodology used in the Nordic countries (Alén et al., 2005). The methodology is based on a volume averaging approach, assuming equal strains in columns and in-between unimproved soil. From the stress at the top of the composite improved block (q = 105 kPa), a stress-strain distribution is assumed with depth using the Boussinesq solution for an elastic half-space and a load split factor to account for the increased composite modulus in the block compared to the underlying soil (Alén et al., 2005). Calculation of this is not outlined in detail herein; however, the depth factor at 10 m depth is ~0.74 given the geometry of the improved ground, i.e., the stress at 10 m depth was estimated to around $105 \times 0.74 \approx 78$ kPa. The strain, at full consolidation, is then given by $\varepsilon_{col} = q_{col}/E_{50,col}$, and it is assumed that the columns have a constant $E_{50,col}$ towards depth. The resulting strain at full consolidation is thus 2,100 $\mu\varepsilon$ at the top of the columns and 1,550 $\mu\varepsilon$ at 10 m depth.

Prediction of consolidation rate is based on an approach where the moduli difference between the unimproved and improved soil is used to calculate a composite coefficient of consolidation ($c_{v,comp}$)

(Wijerathna et al., 2017). Given a coefficient of consolidation ($c_{v,soil}$) of 15 m^2/year for the natural clay and a moduli difference of $E_{50,col}/M_{soil} \approx 4$, the $c_{v,col}$ was estimated to 60 m^2/year, giving a $c_{v,comp}$ of 30 m^2/year. The degree of consolidation is thereby calculated based on Terzaghi's 1D consolidation equation for single sided drainage, giving an average degree of consolidation of around 25% after 6.5 months which is representative for measurement M10.

The resulting strains at measurement M10, based on this analytical model and taking the varying degree of consolidation vs. depth into consideration, are shown with the DSS data in Figure 7. The calculated strains are around 1,700 $\mu\varepsilon$ at 1 m depth, decreasing to around 50 $\mu\varepsilon$ at 10 m depth. The average measured strains in columns L6 and K6 are 890 and 830 $\mu\varepsilon$, respectively, compared to the average calculated of 790 to 950 $\mu\varepsilon$ for the 8 to 10 m column depth. The measured strains thus agree fairly well with the analytical model. The trend of strain vs. depth is also similar to the model; however, weakness zones exhibit higher strain than the model at depths 5 to 8 m, especially in column K6.

The strain rate, based on the consolidation process, is plotted along with the measured strains in Figure 13 from M5, i.e., where the fill elevation reached +15, to the last measurement M10. Although there are considerable simplifications in the 1D consolidation equation and uncertainties in the assumptions made here, the data shows reasonable agreement for column L6. For column K6, the strain rate is lower than the model would suggest. Overall, however, the data indicates that there is ongoing consolidation in the columns, also seen by the dissipating pore pressures, both in column J5 and in the unimproved clay in-between columns (Figure 5). Figure 13 also indicates that the strain coupling is maintained.

4.3 Column variability

The high spatial resolution of the strain data makes it possible to quantify the inherent vertical column variability based on a real strain response. This is advantageous since other estimates of column variability is mostly based on for example penetration tests, which although they give equal high spatial

resolution, the tip resistance is affected by a larger soil volume than the spatial resolution of the data acquisition. In addition, there will be both measurement and transformation errors, the latter as the penetration resistance is transformed to, e.g., strength or stiffness (Phoon & Kulhawy, 1999). Spatial variability is also assessed based on sampling and laboratory tests, but these in turn have low spatial resolution.

Spatial variability is quantitatively described by the mean, the coefficient of variation (COV) and the scale of fluctuation (θ), the latter being defined as the distance over which soil properties are correlated, i.e., the distance of sections with higher-than-average data or lower-than-average data. The θ is often the most difficult parameter to assess since it requires ample data. The vertical scale of fluctuation (θ_v) was here estimated using the variance reduction function (Γ^2) (VanMarcke, 1988; D. Wickremesinghe & Campanella, 2020; D. S. Wickremesinghe, 1989) giving a θ_v of 0.36 m for column L6 and 0.46 m for column K6. The COV was high, 77% and 68% for L6 and K6, respectively. Previous studies of wet deep mixing have shown that θ_v varies considerably, typically between 0.8 m and 8 m, mostly based on sampling and subsequent laboratory tests (Honjo, 1982; Y. Liu et al., 2019). For the dry deep mixing method, θ_v has been estimated between 0.2 and 1.4 m, mostly based on penetration tests (Al-Naqshabandy & Larsson, 2013; Bergman et al., 2013; Wong et al., 2024).

The θ_v of 0.36–0.46 m presented herein is thus in the lower range, possibly due to the higher spatial resolution of the data. However, comparing different sites is challenging since the column variability is highly dependent on the ground conditions, soil properties and mixing execution and efficiency, all of which affects the binder distribution and hence the column variability. Nevertheless, this has implications for the utilisation of DSS in deep mixing applications. Despite the relatively low θ_v and high COV, the bond strength was sufficient to maintain the strain gradients forced on the sensor. Thus, most other deep mixing applications with a larger θ_v and lower COV should also be able to maintain the strain gradient given equal or higher shear strengths of the improved columns.

5. CONSIDERATIONS FOR PRACTICE

5.1 Specific challenges in deep mixing

The application of DFOS in ground improvement by deep mixing differ considerably from other applications such as piles or anchors, particularly for strain sensing. For piles and anchors, sensors are attached to or casted into structural elements which are subsequently installed in the ground, and hence, sensors can also easily be protected to avoid damage. Further, the physical connection or contact between the sensor and the element can be designed to ensure strain compatibility between the sensor and the concrete or steel element. In deep mixing, new challenges arise as there are no structural elements to attach a sensor, meaning that the installation must be done by pushing down the sensors after column execution. The considerably lower stiffness of deep mixed columns compared to, e.g., concrete piles, requires that the sensor stiffness and diameter and column properties must be chosen or designed to allow for sufficient strain coupling, as discussed in section 4.1 above. In particular, this can be challenging since column properties can vary greatly depending on, e.g., ground conditions, binder quantities and mixing procedures. However, even with a proper choice of sensor type and obtained column properties, strain coupling cannot be guaranteed unless an installation procedure is used which gives full physical contact between the sensor and the improved column. A key challenge is the weighting between lowest possible sensor stiffness and smallest sensor diameter whilst having sufficient robustness and durability to avoid damage during installation and the intended lifespan.

5.2 Installation aspects

Installation of DFOS sensors in deep mixed columns can be done by a rod with the sensor either on the outside, or with the sensor on the inside so that the rod acts as a protective casing. The sensor needs to be attached to a sacrificial anchor during withdrawal of the rod. Further, the sensor can be installed in freshly mixed column, or after some curing, requiring predrilling and subsequent grouting of the

borehole. The latter has been done for DSS in natural soil deposits (Yeskoo & Soga, 2022; Zhang et al., 2018).

This project attempted to install the sensors in freshly mixed columns with the sensor on the outside of the rod. This method was chosen since it was believed that the freshly mixed columns would be in a semi-liquid state to facilitate this, and so that the sensors would be in immediate contact with the column material as it cured over time. However, the freshly mixed columns were still relatively stiff due to the high remoulded shear strength of the clay and hence the columns, giving a high resistance during penetration. The high resistance unfortunately caused breakage of some sensors, which later interrogations revealed occurred at the end of the sensors, i.e., were the forces would be greatest. Notably, the EpsilonSensors used herein was 3 mm in diameter with an axial stiffness of 3 GPa. However, this also meant that the surviving sensors were naturally pre-tensioned as a result of this installation process, and thus no further pre-tensioning was done to avoid damage. It was considered whether the water content of the slurry should be increased, but that could risk not achieving the target design strength as an increased water content reduces strength and stiffness.

In general terms, it is believed that for soft freshly mixed columns, DFOS sensors should be installed at an early stage, with or without a casing. The freshly mixed column must collapse around the sensor as the rod is withdrawn to obtain full physical contact where curing ensures optimal bond strength. If the freshly mixed column is too stiff, or if the column has cured, grouting might be required to obtain full physical contact. The grout must then be designed to obtain similar characteristics as the improved column.

It is recommended that cone penetration tests are performed in the columns immediately before installation of DFOS sensors. This will not only serve as information to make potential adjustments of the sensor installation procedure, but also provide information of column properties such as indications of

406 strength and stiffness as well as spatial variability which can be valuable for later strain data
407 interpretation. Furthermore, pre-tensioning of the sensors should be performed. However, this can be
408 difficult depending on site conditions, and care must be taken to avoid damaging the sensors during pre-
409 tensioning. In the case of pushing in without casing, a natural pre-tensioning might be obtained as in the
410 case presented herein.

411 **6. CONCLUSIVE REMARKS**

412 This paper has presented a novel case study of distributed fiber optic strain sensing in ground
413 improvement by deep mixing. Sensors were installed in columns, and the improved ground was
414 subsequently loaded with an embankment. Frequent interrogation of the DSS sensors revealed that:

415 • Strains after around 6.5 months consolidation ranged from around 150 $\mu\varepsilon$ to around 3,900 $\mu\varepsilon$.
416 The peak values correspond to weakness zones with higher compressibility.

417 • The sensors showed highly responsive changes in strain rate as additional load was applied.
418 Current design methodology agreed well with the measured strain magnitude when
419 disregarding clear weakness zones, and strain rate due to consolidation.

420 • Zones with varying compressibility creates strain gradients in the sensor, and thus also stress
421 gradients. To avoid slippage, this stress gradient must be in equilibrium with the interface shear
422 stress at the sensor's periphery. The mobilised interface shear stress was shown to be maximum
423 around 50% of the estimated bond strength, strongly indicating that strain coupling was
424 achieved.

425 • The distributed strain data revealed a high vertical column variability. The coefficient of
426 variation was large, around 68–77%, and the scale of fluctuation was estimated to 0.36–0.46 m.
427 This is in the lower range of previous experiences.

The results presented in this paper demonstrate that distributed fiber optic sensing is applicable to deep mixing. The technology can provide distributed strain profiling that previously has not been possible in deep mixed columns, giving new insights into the performance of this type of ground improvement.

Further research needs primarily involves soil-sensor strain coupling of binder-improved soils, in particular how this is affected by bond strength, confining pressure and cementitious bonds created at the interface.

DATA AVAILABILITY STATEMENT

Some or all data, models, or code that support the findings of this study are available from the corresponding author upon reasonable request.

ACKNOWLEDGEMENTS

The distributed fiber optic sensing work was funded by the Research Council of Norway, GBV project number 20230067. Time spent for data processing was funded by the Research Council of Norway through the project 'GOAL—Green Soil Stabilisation', grant number 328767. The authors highly appreciate the assistance during field work by Espen Andersen Torsæter at the Norwegian University of Science and Technology, and Martin Keiserås Haugen and Ole Wostryck Eiesland at the Norwegian Geotechnical Institute. The assistance and patience from the main contractor Veidekke Entreprenør AS and the earth works contractor Tverås Maskin & Transport AS is also appreciated. The authors are thankful to the anonymous reviewers and Prof. Mike Long at University College Dublin for valuable comments on the manuscript.

REFERENCES

Alén, C., Baker, S., Bengtsson, P.-E., & Sällfors, G. (2005). Lime/Cement column stabilised soil - A new model for settlement calculation. Deep Mixing '05, 205–212.

Al-Naqshabandy, M. S., & Larsson, S. (2013). Effect of Uncertainties of Improved Soil Shear Strength on the Reliability of Embankments. Journal of Geotechnical and Geoenvironmental Engineering, 139(4), 619–632. https://doi.org/10.1061/(asce)gt.1943-5606.0000798

Ansari, F., & Libo, Y. (1998). Mechanics of bond and interface shear transfer in optical fiber sensors. 385–394.

Bache, B. K., Wiersholm, P., Paniagua, P., & Emdal, A. (2022). Effect of Temperature on the Strength of Lime–Cement Stabilized Norwegian Clays. Journal of Geotechnical and Geoenvironmental Engineering, 148(3). https://doi.org/10.1061/(asce)gt.1943-5606.0002699

Bado, M. F., & Casas, J. R. (2021). A review of recent distributed optical fiber sensors applications for civil engineering structural health monitoring. In Sensors (Vol. 21, Issue 5, pp. 1–83). MDPI AG. https://doi.org/10.3390/s21051818

Bednarski, Ł., Sieńko, R., Howiacki, T., & Zuziak, K. (2022). The Smart Nervous System for Cracked Concrete Structures: Theory, Design, Research, and Field Proof of Monolithic DFOS-Based Sensors. Sensors 2022, Vol. 22, Page 8713, 22(22), 8713. https://doi.org/10.3390/S22228713

Bergman, N., Al-Naqshabandy, M. S., & Larsson, S. (2013). Variability of strength and deformation properties in lime-cement columns evaluated from CPT and KPS measurements. Georisk, 7(1), 21–36. https://doi.org/10.1080/17499518.2013.763571

Chamoin, L., Farahbakhsh, S., & Poncelet, M. (2022). An educational review on distributed optic fiber sensing based on Rayleigh backscattering for damage tracking and structural health monitoring.

Chapeleau, X., & Bassil, A. (2021). A general solution to determine strain profile in the core of distributed fiber optic sensors under any arbitrary strain fields. Sensors, 21(16). https://doi.org/10.3390/s21165423

Chen, C., Zhang, G., Zornberg, J. G., Morsy, A. M., Zhu, S., & Zhao, H. (2018). Interface behavior of tensioned bars embedded in cement-soil mixtures. Construction and Building Materials, 186, 840–853. https://doi.org/10.1016/J.CONBUILDMAT.2018.07.211

Chen, W., Hong, C., Chena, X., Luoa, G., & Sua, D. (2023). Comparative analysis of anchor cables in pullout tests using distributed fiber optic sensors. Canadian Geotechnical Journal, 60(12), 1861–1876. https://doi.org/10.1139/cgj-2022-0455

Ding, Z., Wang, C., Liu, K., Jiang, J., Yang, D., Pan, G., Pu, Z., & Liu, T. (2018). Distributed optical fiber sensors based on optical frequency domain reflectometry: A review. In Sensors (Switzerland) (Vol. 18, Issue 4). MDPI AG. https://doi.org/10.3390/s18041072

Hartog, A. H. (2017). An introduction to distributed optical fibre sensors. CRC Press.

Honjo, Y. (1982). A probabilistic approach to evaluate shear strength of heterogeneous stabilized ground by deep mixing method. Soils and Foundations, 22(1), 23–38.

Hov, S., & Larsson, S. (2023). Strength and Stiffness Properties of Laboratory-Improved Soft Swedish Clays. International Journal of Geosynthetics and Ground Engineering, 9(1). https://doi.org/10.1007/s40891-023-00432-3

Howiacki, T., Sieńko, R., Bednarski, Ł., & Zuziak, K. (2023). Crack Shape Coefficient: Comparison between Different DFOS Tools Embedded for Crack Monitoring in Concrete. Sensors 2023, Vol. 23, Page 566, 23(2), 566. https://doi.org/10.3390/S23020566

Kechavarzi, C., Soga, K., de Battista, N., Pelecanos, L., Elshafie, M., & Mair, R. J. (2016). Distributed Fibre Optic Strain Sensing for Monitoring Civil Infrastructure. Thomas Telford Limited.

Kitazume, M. (2022). Quality Control and Assurance of the Deep Mixing Method. CRC Press - Taylor & Francis Group.

Kitazume, M., & Terashi, M. (2013). The Deep Mixing Method. Taylor & Francis Group.

Larsson, S. (2005). State of Practice Report - Execution, monitoring and quality control. International Conference on Deep Mixing: Best Practice and Recent Advances, 732–785.

Lin, S.-Q., Tan, D.-Y., Leung, Y. F., Yin, J.-H., Li, I., Sze, E. H. Y., Lo, F. L. C., Kan, H.-S., Wong, T. C. W., & Chan, E. Y. M. (2023). Fiber-Optic Monitoring of a Twin Circular Shaft Excavation: Development of Circumferential Forces and Bending Moments in Diaphragm Walls. Journal of Geotechnical and Geoenvironmental Engineering, 149(12). https://doi.org/10.1061/jggefk.gteng-11211

Liu, J., Song, Z., Lu, Y., Bai, Y., Qian, W., Kanungo, D. P., Chen, Z., & Wang, Y. (2019). Monitoring of vertical deformation response to water draining–recharging conditions using BOFDA-based distributed optical fiber sensors. Environmental Earth Sciences, 78(14). https://doi.org/10.1007/s12665-019-8409-7

Liu, Y., He, L. Q., Jiang, Y. J., Sun, M. M., Chen, E. J., & Lee, F. H. (2019). Effect of in situ water content variation on the spatial variation of strength of deep cement-mixed clay. Geotechnique, 69(5), 391–405. https://doi.org/10.1680/jgeot.17.P.149

Mohamad, H., Soga, K., Pellew, A., & Bennett, P. J. (2011). Performance Monitoring of a Secant-Piled Wall Using Distributed Fiber Optic Strain Sensing. Journal of Geotechnical and Geoenvironmental Engineering, 137(12), 1236–1243. https://doi.org/10.1061/(asce)gt.1943-5606.0000543

Monsberger, C. M., Lienhart, W., & Hayden, M. (2020). Distributed fiber optic sensing along driven ductile piles: Design, sensor installation and monitoring benefits. Journal of Civil Structural Health Monitoring, 10(4), 627–637. https://doi.org/10.1007/s13349-020-00406-3

Paniagua, P., Bache, B. K., Karlsrud, K., & Lund, A. K. (2022). Strength and stiffness of laboratory-mixed specimens of stabilised Norwegian clays. Proceedings of the Institution of Civil Engineers: Ground Improvement, 175(2), 150–163. https://doi.org/10.1680/jgrim.19.00051

Pelecanos, L., Soga, K., Elshafie, M. Z. E. B., de Battista, N., Kechavarzi, C., Gue, C. Y., Ouyang, Y., & Seo, H.-J. (2018). Distributed Fiber Optic Sensing of Axially Loaded Bored Piles. Journal of Geotechnical and

Geoenvironmental Engineering, 144(3), 04017122. https://doi.org/10.1061/(ASCE)GT.1943-5606.0001843

Phoon, K.-K., & Kulhawy, F. H. (1999). Characterization of geotechnical variability.

Piątek, B., Howiacki, T., Kulpa, M., Siwowski, T., Sieńko, R., & Bednarski, Ł. (2023). Strain, crack, stress and shape diagnostics of new and existing post-tensioned structures through distributed fibre optic sensors. Measurement, 221, 113480. https://doi.org/10.1016/J.MEASUREMENT.2023.113480

Seo, H. (2020). Monitoring of CFA pile test using three dimensional laser scanning and distributed fiber optic sensors. Optics and Lasers in Engineering, 130. https://doi.org/10.1016/j.optlaseng.2020.106089

Sienko, R., Bednarski, L., Kanty, P., & Howiacki, T. (2018). Application of Distributed Optical Fibre Sensor for Strain and Temperature Monitoring within Continuous Flight Auger Columns. IOP Conference Series: Earth and Environmental Science, 221(1). https://doi.org/10.1088/1755-1315/221/1/012006

Soga, K., & Luo, L. (2018). Distributed fiber optics sensors for civil engineering infrastructure sensing. Journal of Structural Integrity and Maintenance, 3(1), 1–21. https://doi.org/10.1080/24705314.2018.1426138

Sun, L., Li, C., Zhang, C., Liang, T., & Zhao, Z. (2019). The strain transfer mechanism of fiber bragg grating sensor for extra large strain monitoring. Sensors (Switzerland), 19(8). https://doi.org/10.3390/s19081851

VanMarcke, E. (1988). Random Fields: Analysis and Synthesis. The MIT Press.

Wang, D., Abriak, N. E., & Zentar, R. (2015). One-dimensional consolidation of lime-treated dredged harbour sediments. European Journal of Environmental and Civil Engineering, 19(2), 199–218. https://doi.org/10.1080/19648189.2014.939309

Wang, H., & Dai, J. G. (2019). Strain transfer analysis of fiber Bragg grating sensor assembled composite structures subjected to thermal loading. Composites Part B: Engineering, 162, 303–313. https://doi.org/10.1016/j.compositesb.2018.11.013

Wickremesinghe, D., & Campanella, R. G. (2020). Scale of fluctuation as a descriptor of soil variability. Probabilistic Methods in Geotechnical Engineering, 233–239. https://doi.org/10.1201/9781003077749-22

Wickremesinghe, D. S. (1989). Statistical characterization of soil profiles using in situ tests [PhD Thesis]. University of British Colombia.

Wijerathna, M., Liyanapathirana, D. S., & Jian Leo, C. (2017). Analytical Solution for the Consolidation Behavior of Deep Cement Mixed Column–Improved Ground. International Journal of Geomechanics, 17(9). https://doi.org/10.1061/(asce)gm.1943-5622.0000954

549 Wong, D. Y. C., Sadasivan, V., Isaksson, J., Karlsson, A., & Dijkstra, J. (2024). Trans-scale spatial variability
550 of lime-cement mixed columns. Construction and Building Materials, 417.
551 https://doi.org/10.1016/j.conbuildmat.2024.135394

552 Xu, D. sheng, Yin, J. hua, & Liu, H. bei. (2018). A new measurement approach for deflection monitoring
553 of large-scale bored piles using distributed fiber sensing technology. Measurement: Journal of the
554 International Measurement Confederation, 117, 444–454.
555 https://doi.org/10.1016/j.measurement.2017.12.032

556 Yeskoo, A., & Soga, K. (2022). Distributed Fiber Optic Monitoring of Ground Settlement. 11th
557 International Symposium Field Monitoring in Geomechanics, 1–7.

558 Zhang, C. C., Shi, B., Gu, K., Liu, S. P., Wu, J. H., Zhang, S., Zhang, L., Jiang, H. T., & Wei, G. Q. (2018).
559 Vertically Distributed Sensing of Deformation Using Fiber Optic Sensing. Geophysical Research Letters,
560 45(21). https://doi.org/10.1029/2018GL080428

561

Table 1. Construction scheme and testing programme

Time after column execution (weeks)	Date	Time after DFOS reference (days)	Site activities [1)]	Surface level
-	2023-06-14–2023-07-21	-	Columns execution (duration around 5 weeks). Installation of DSS and Pz in column J5	+10.5
5-10	2023-08-24	0	Reference reading DSS	+10.5
6-11	2023-09-01	8	Measurement M1	+11.5
7-12	2023-09-08	15	Measurement M2	+12.5
8-13	2023-09-15	22	Measurement M3, reference reading settlement plates (SP6–SP8)	+12.5
10-15	2023-09-29	36	Measurement M4	+13.2
12-17	2023-10-12	49	Measurement M5	+15.0
14-19	2023-10-27	64	Measurement M6	+15.0
15-20	2023-10-28	-	Installation of Pz1 and Pz2	+15.0
18-23	2023-11-22	90	Measurement M7	+15.0
22-27	2023-12-21	119	Measurement M8	+15.0
28-33	2024-01-31	160	Measurement M9	+16.0
33-38	2024-03-06	195	Measurement M10	+16.0

1) Measurements are designated “M1” to “M10” to indicate the number of measurements since reference reading.

Figure 1a

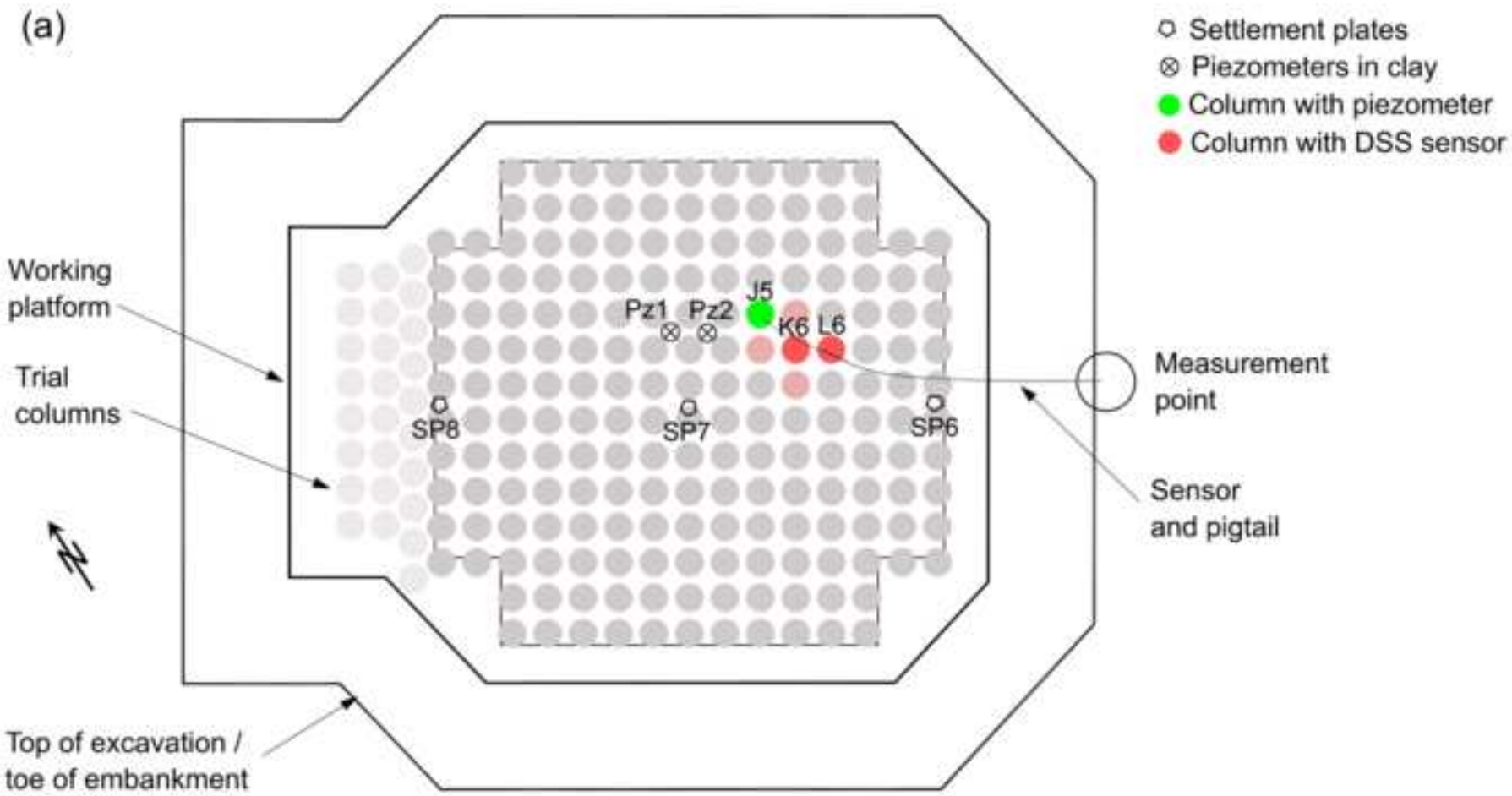

Figure 1b

Click here to access/download;Figure;Figure 1b.tiff

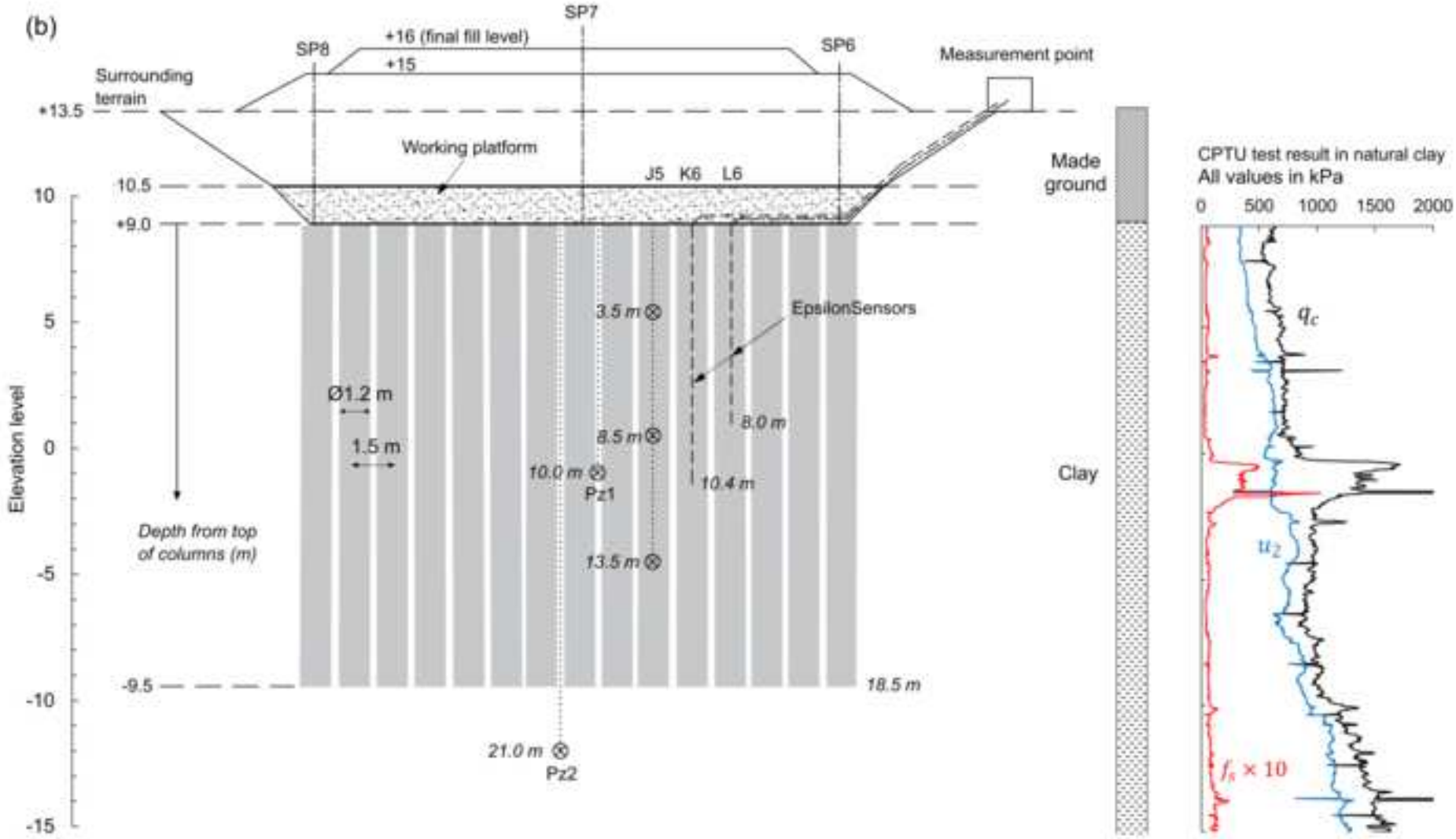

Figure 2

Figure 3

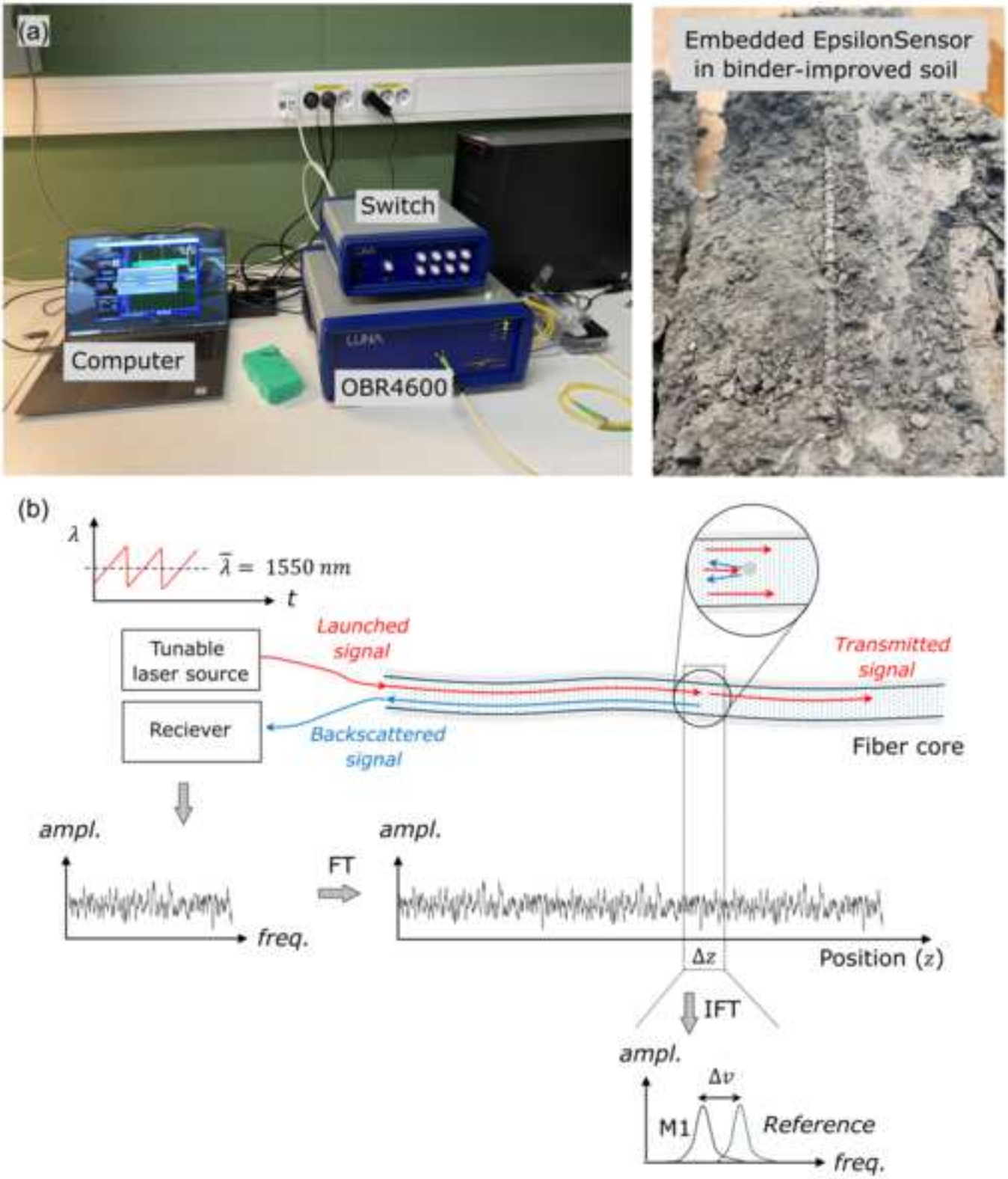

Figure 4

Click here to access/download;Figure;Figure 4.tiff

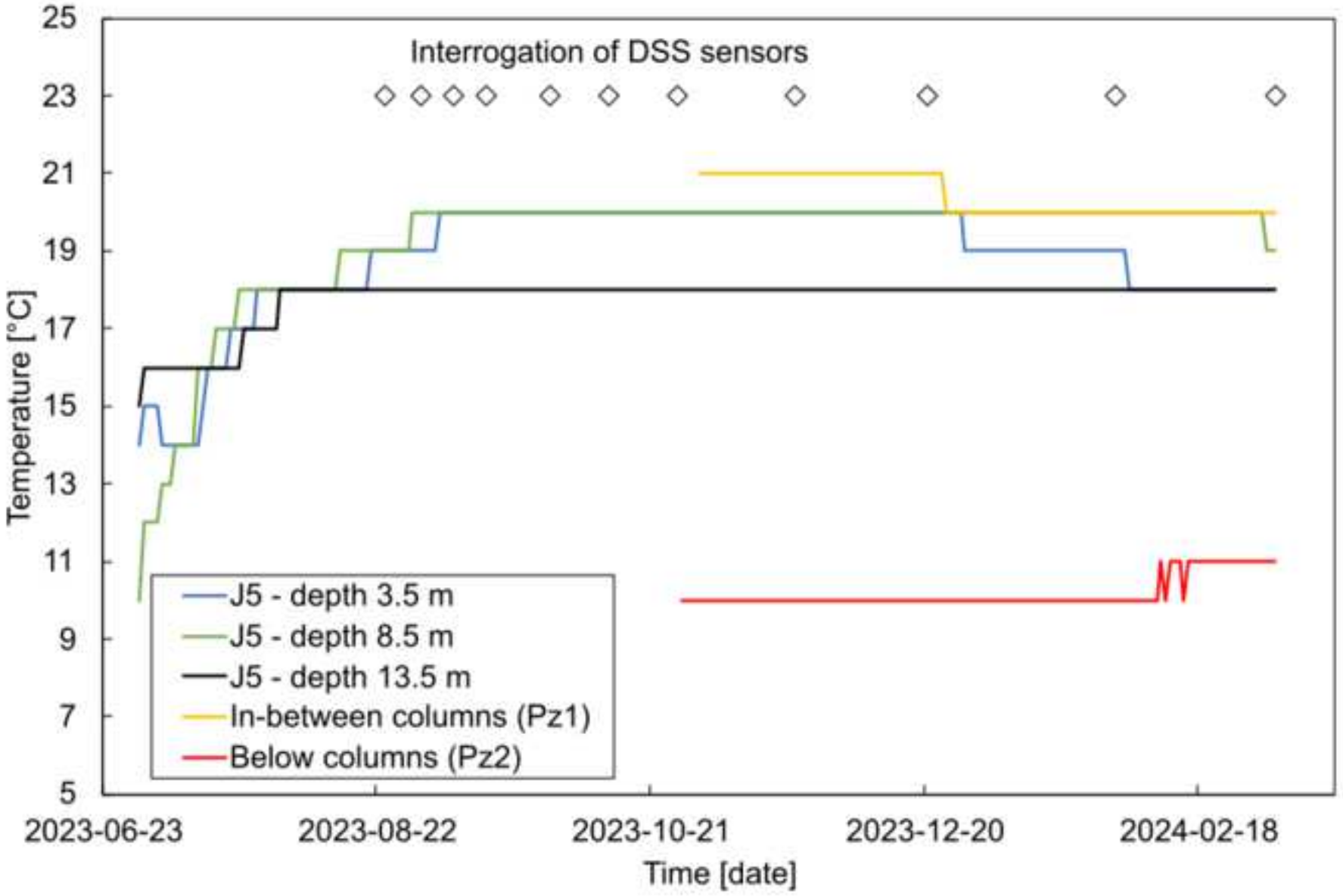

Figure 5

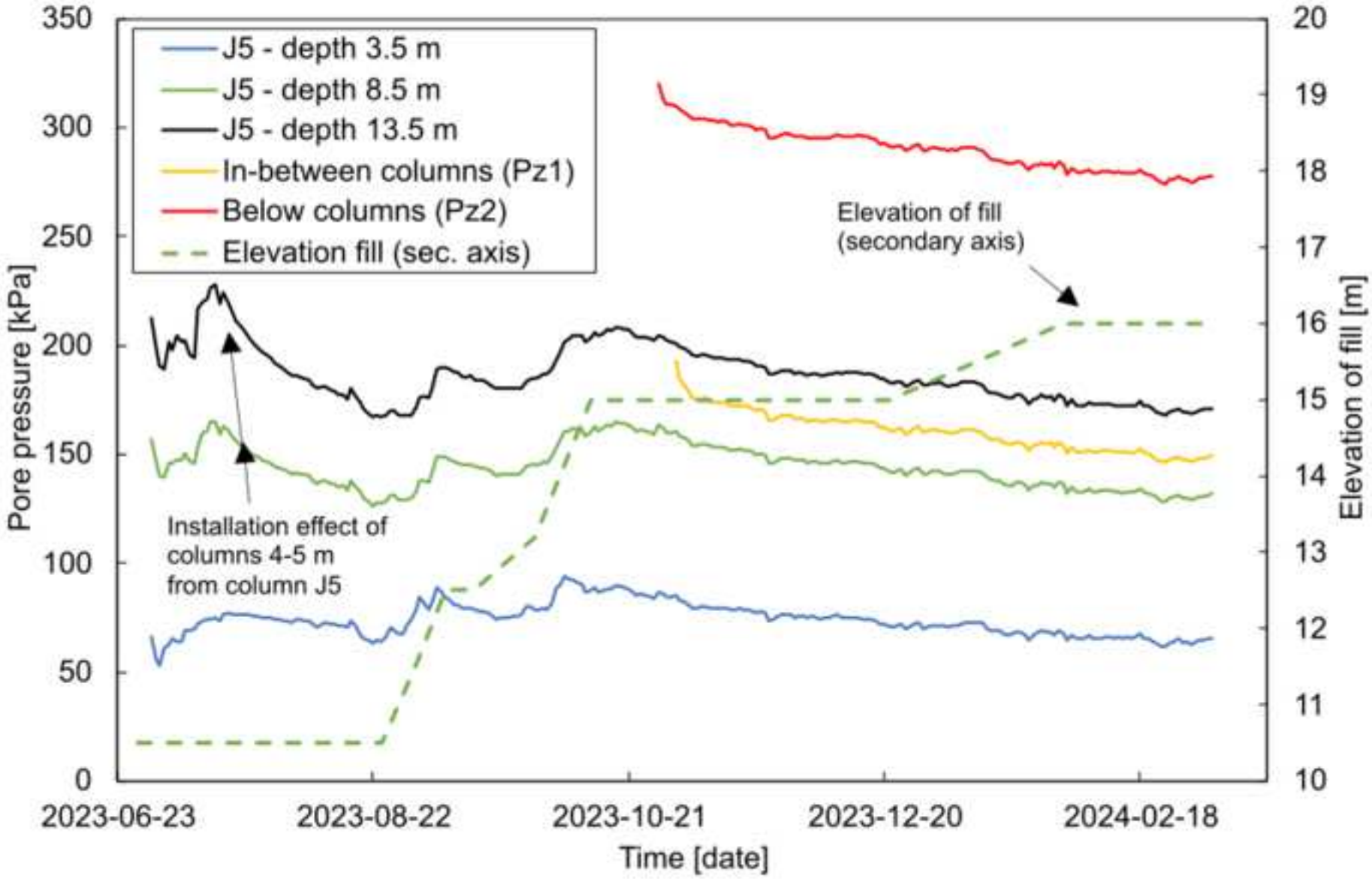

Figure 6

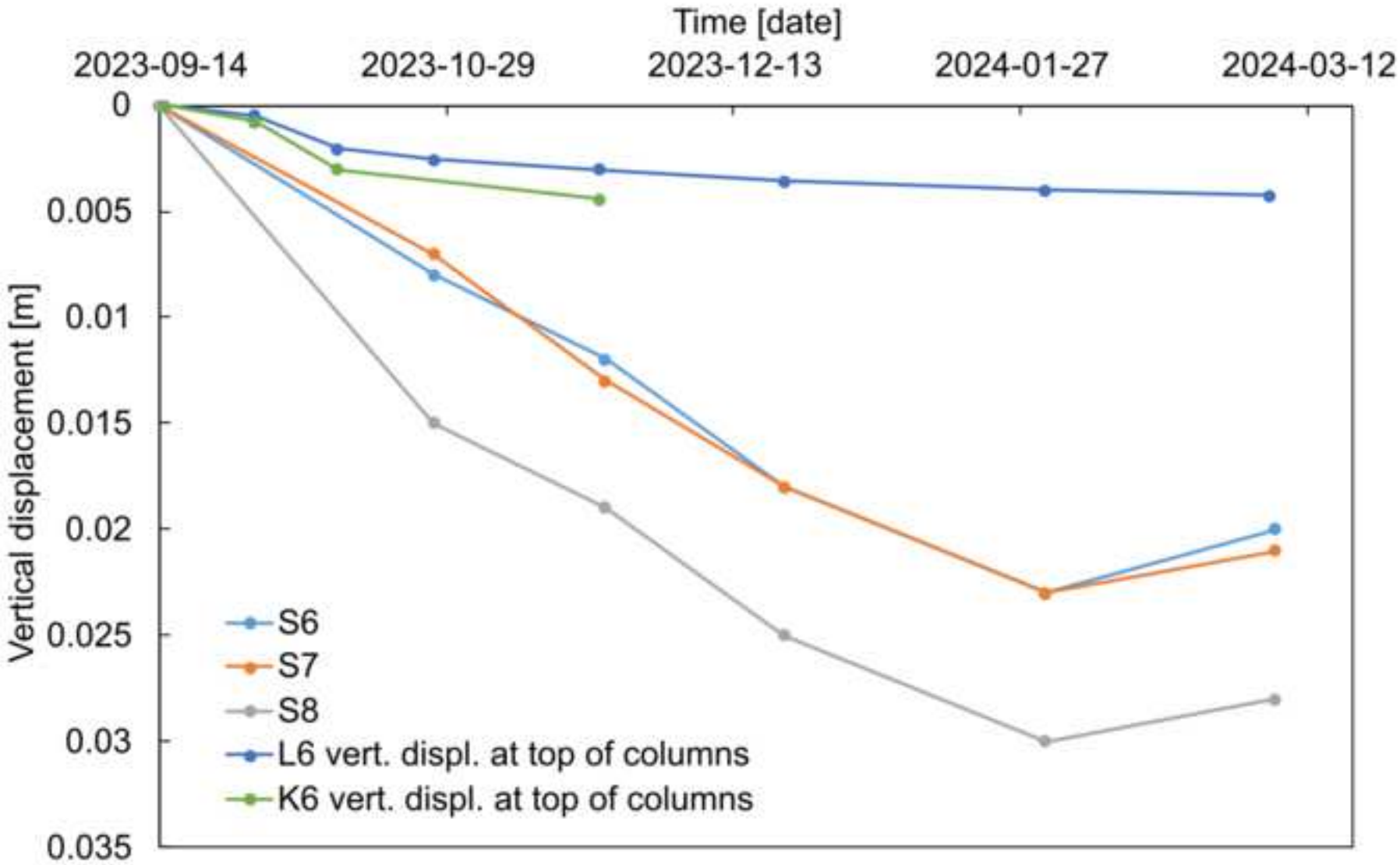

Figure 7

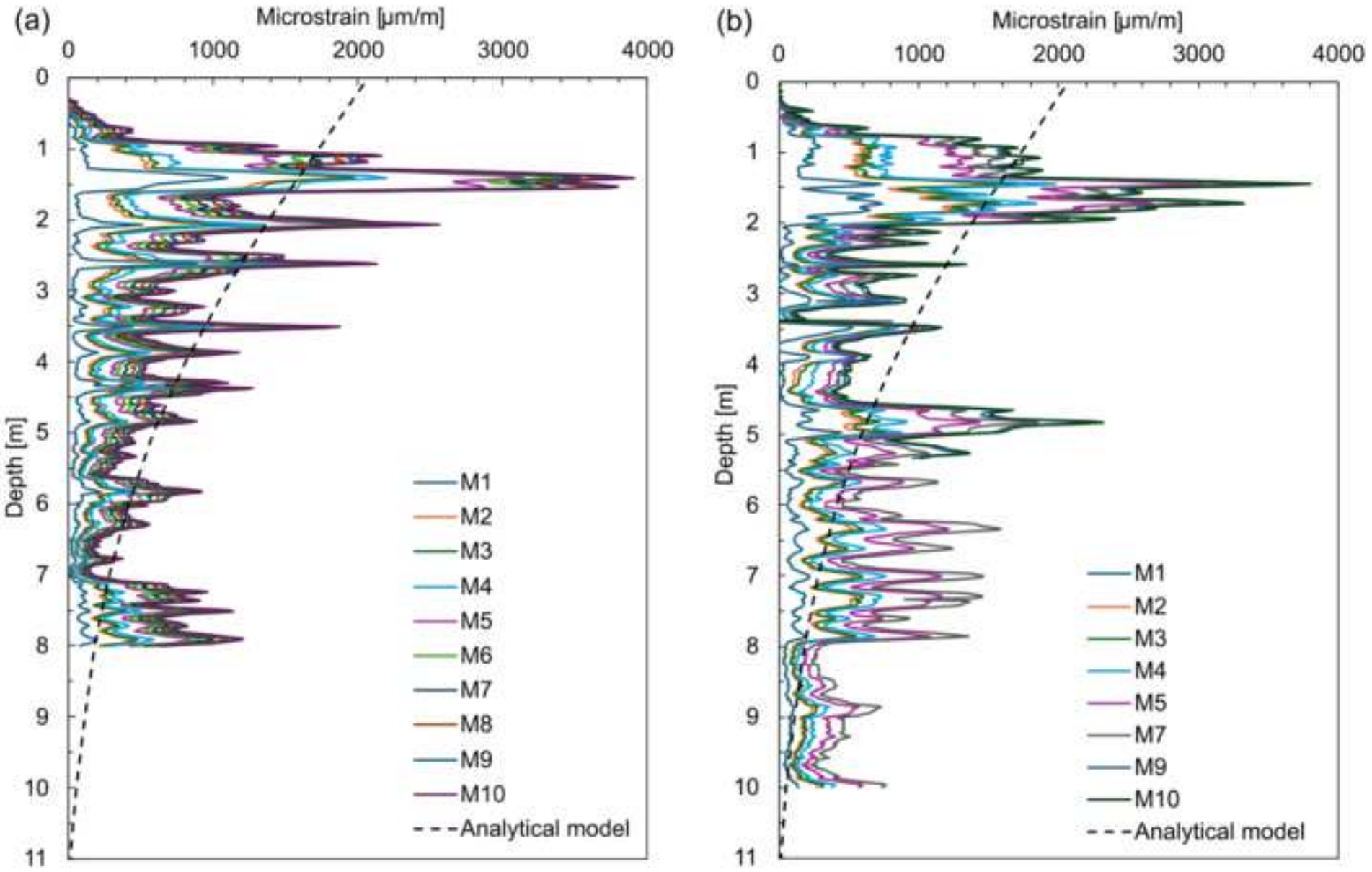

Figure 8

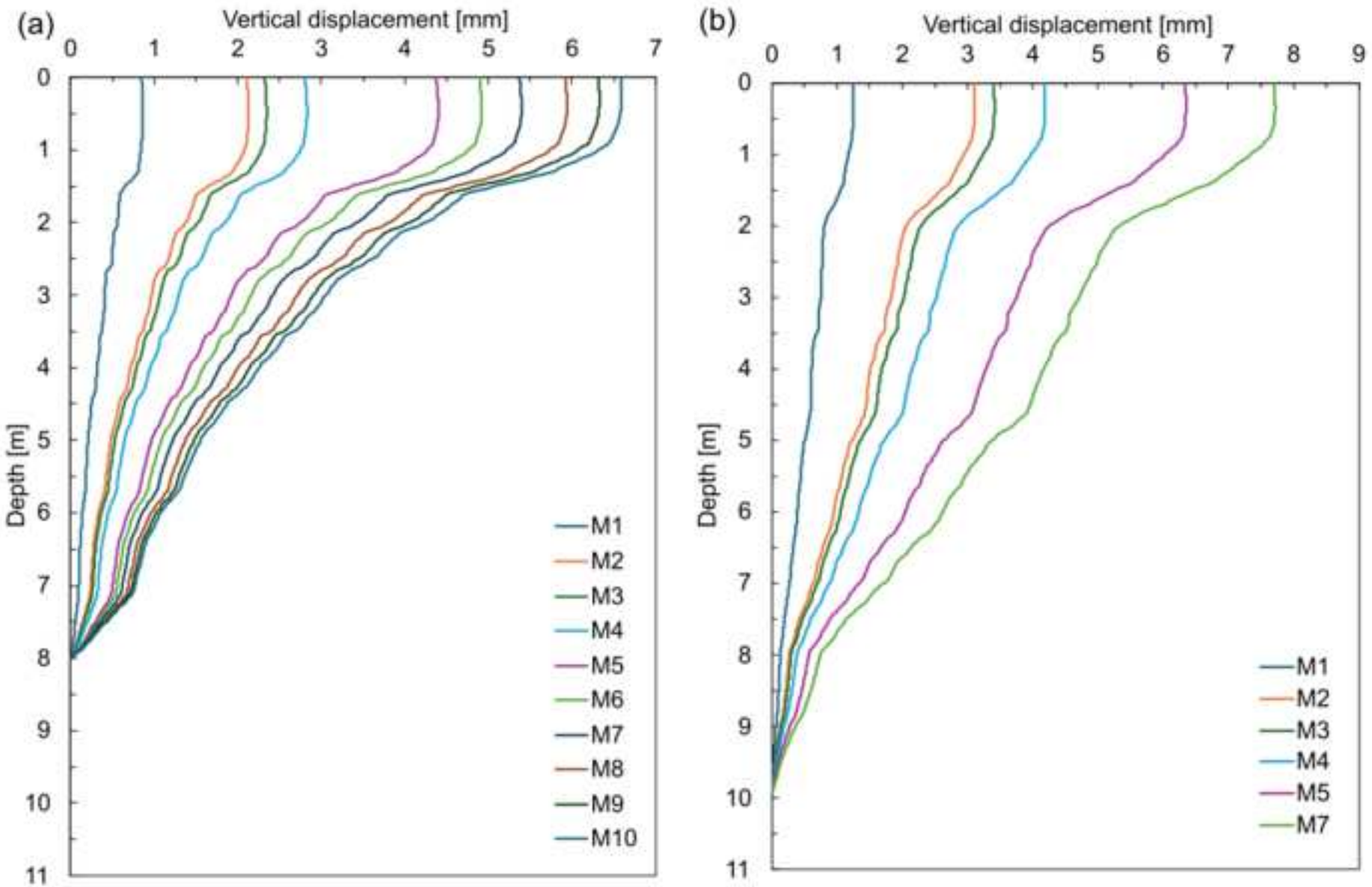

Figure 9

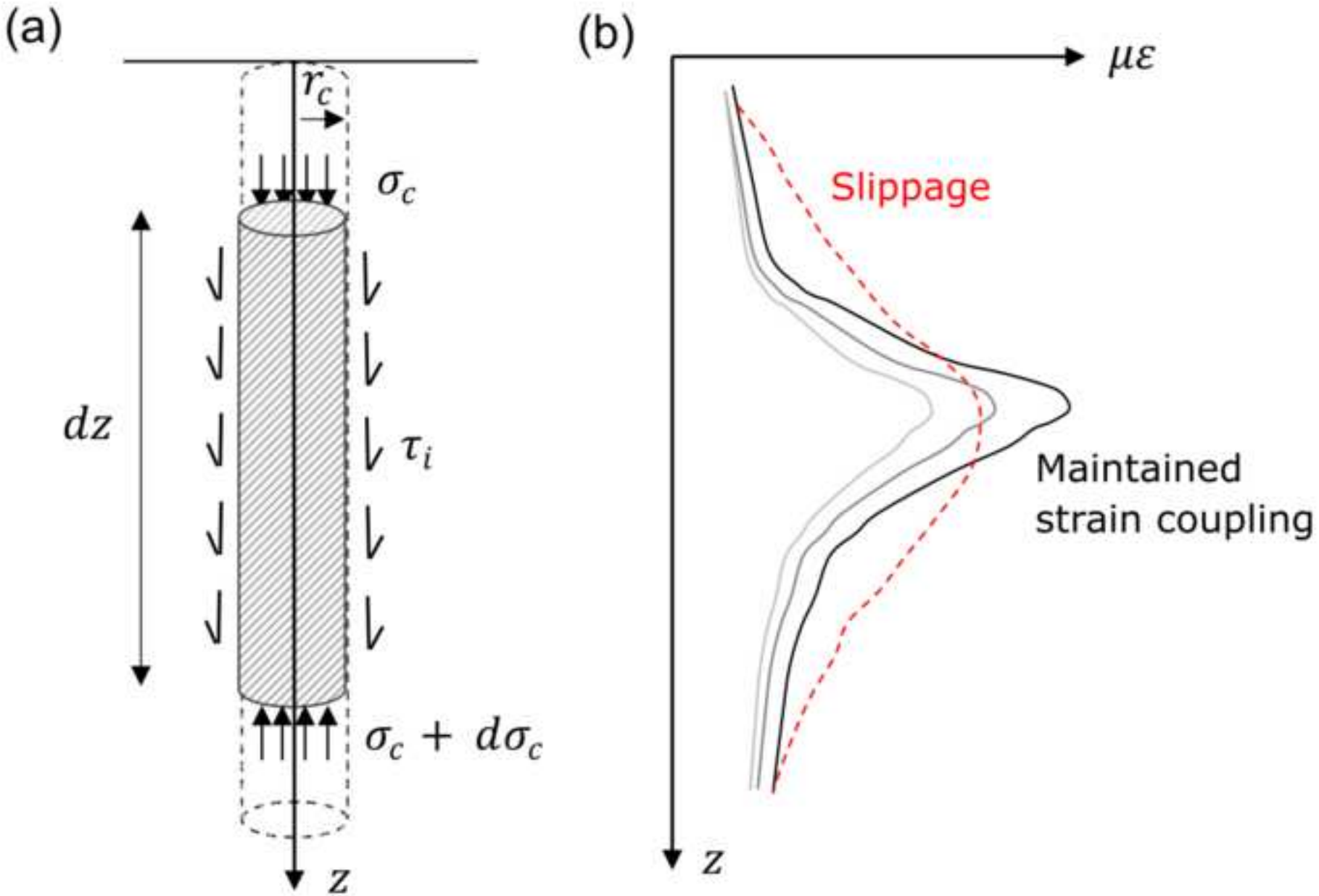

Figure 10

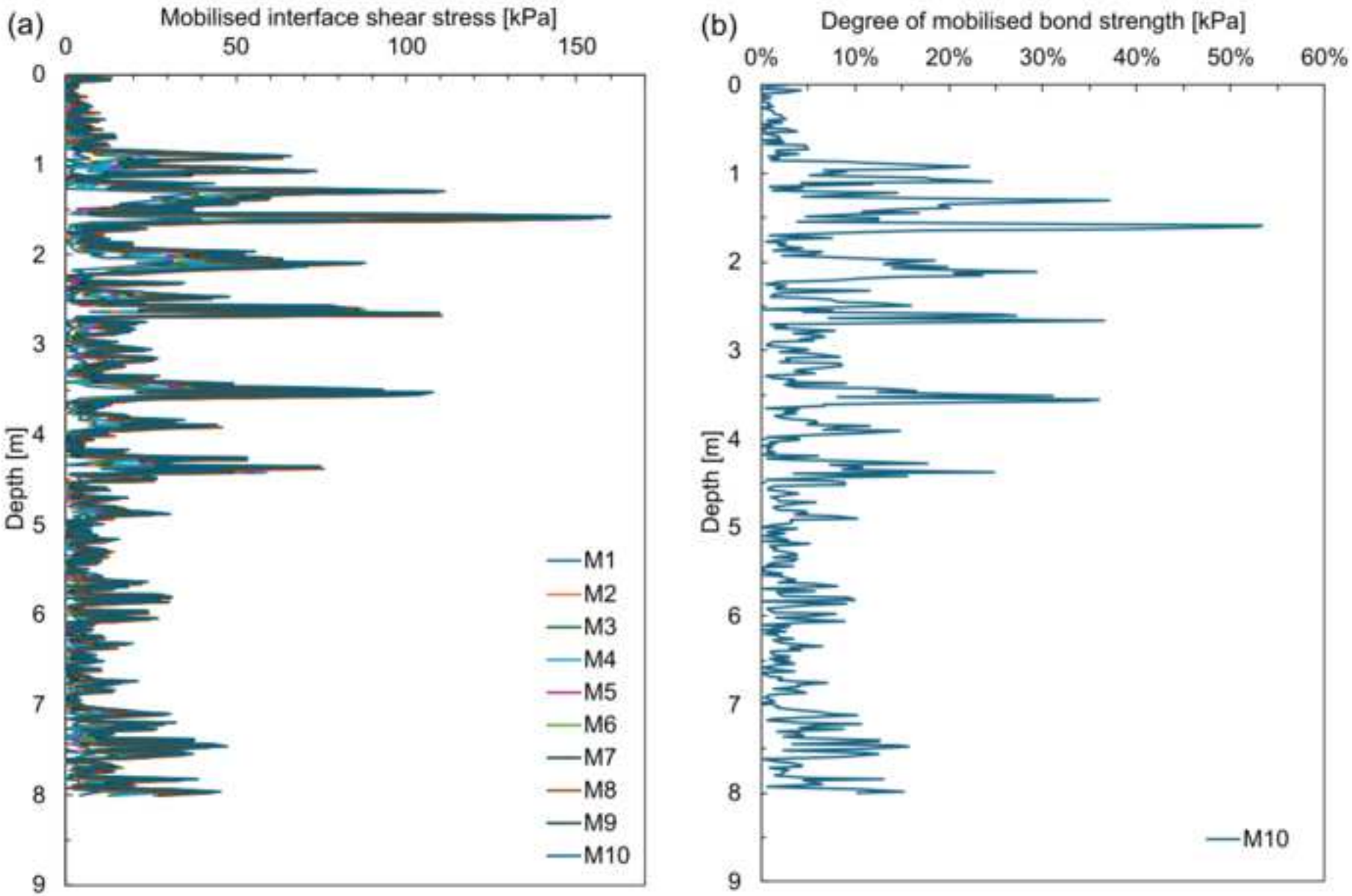

Figure 11

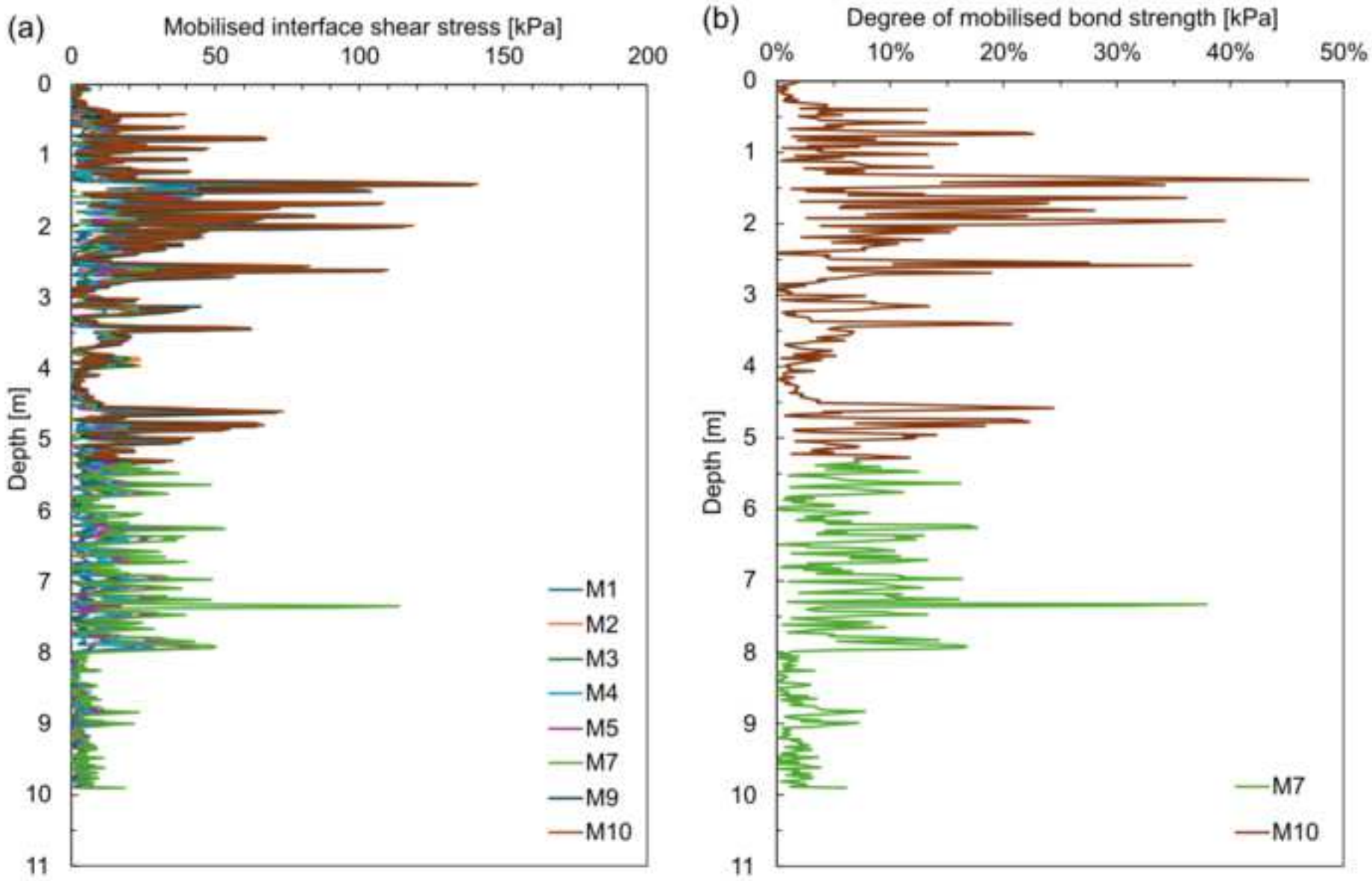

Figure 12

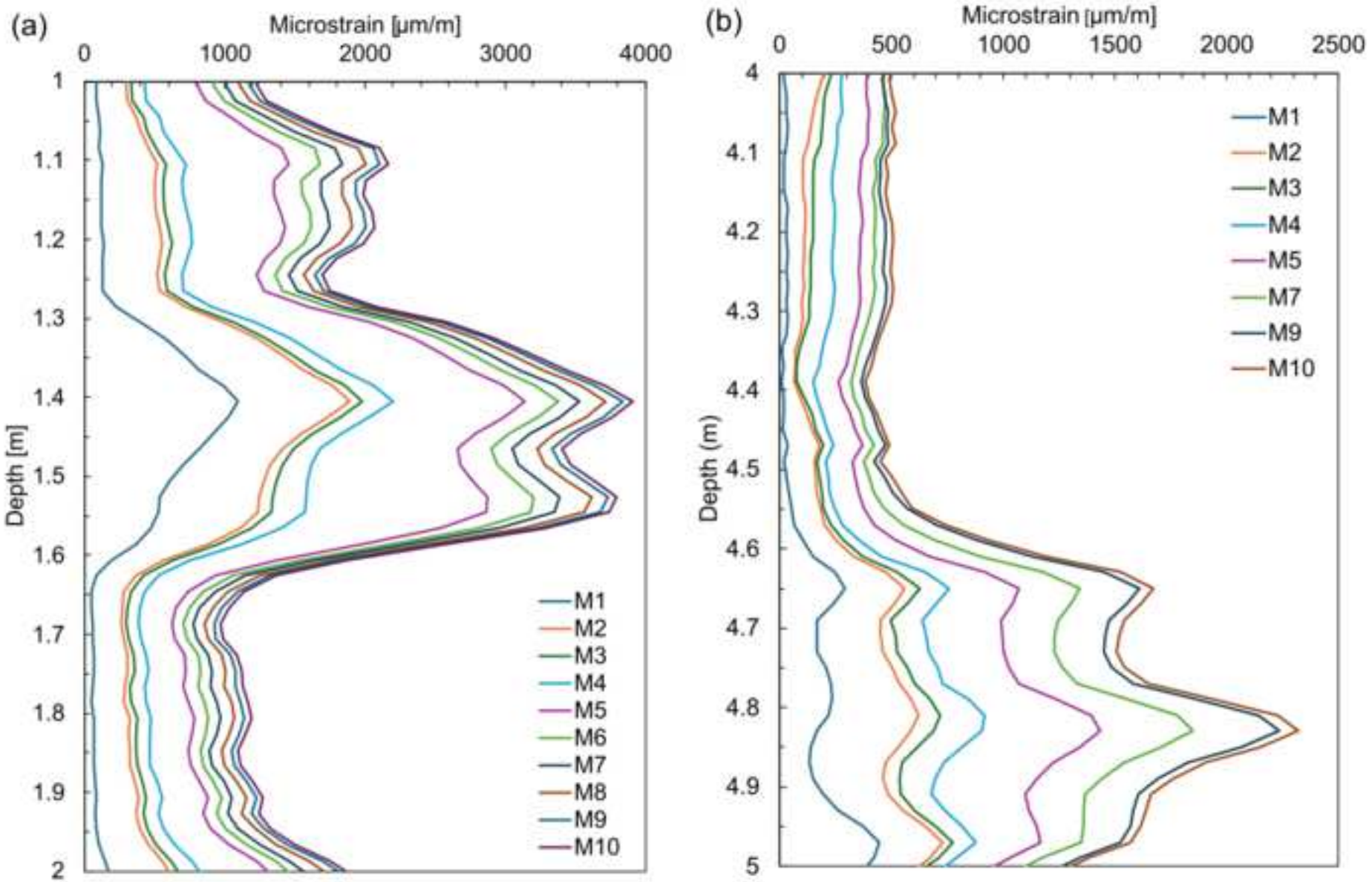

Figure 13a

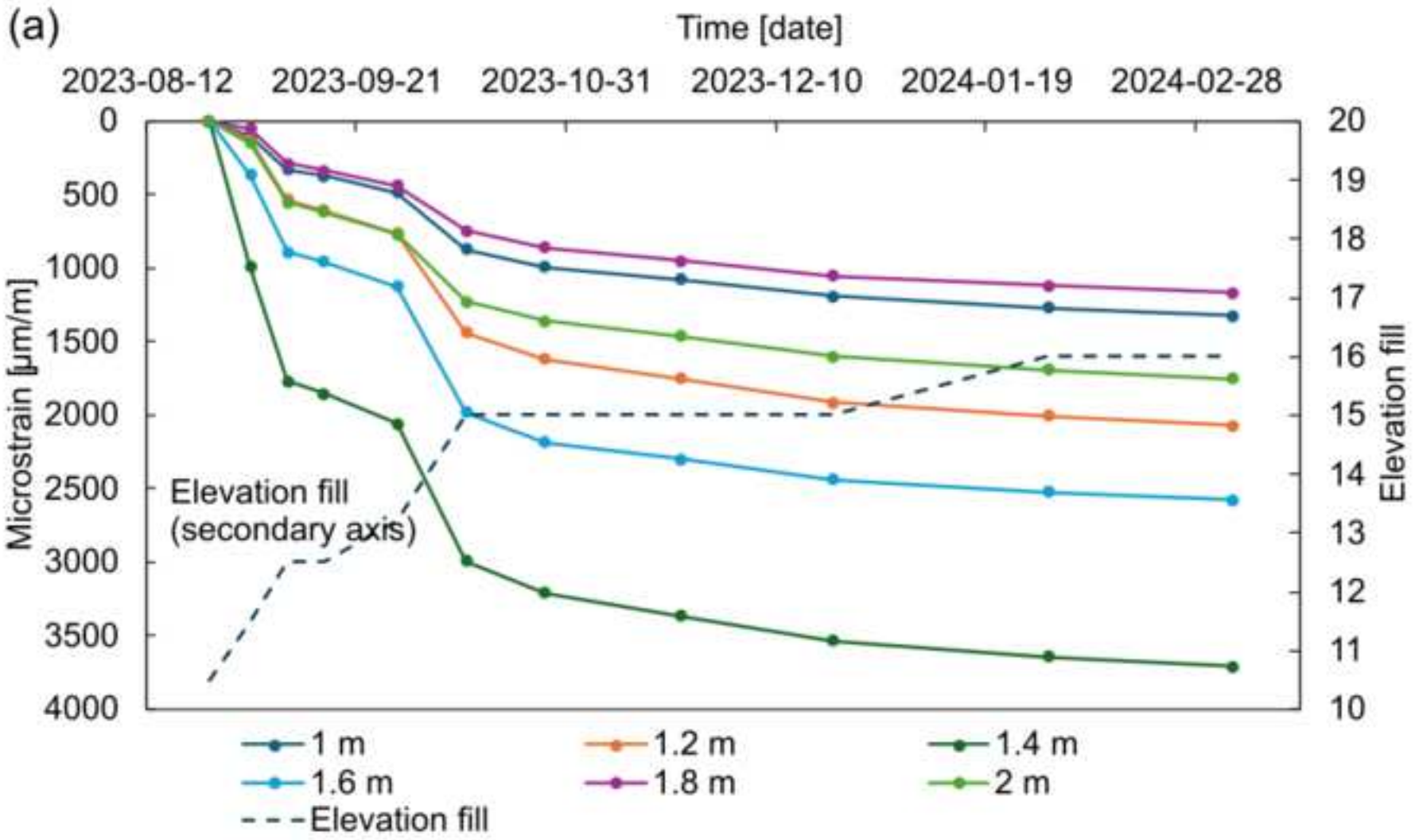

Figure 13b

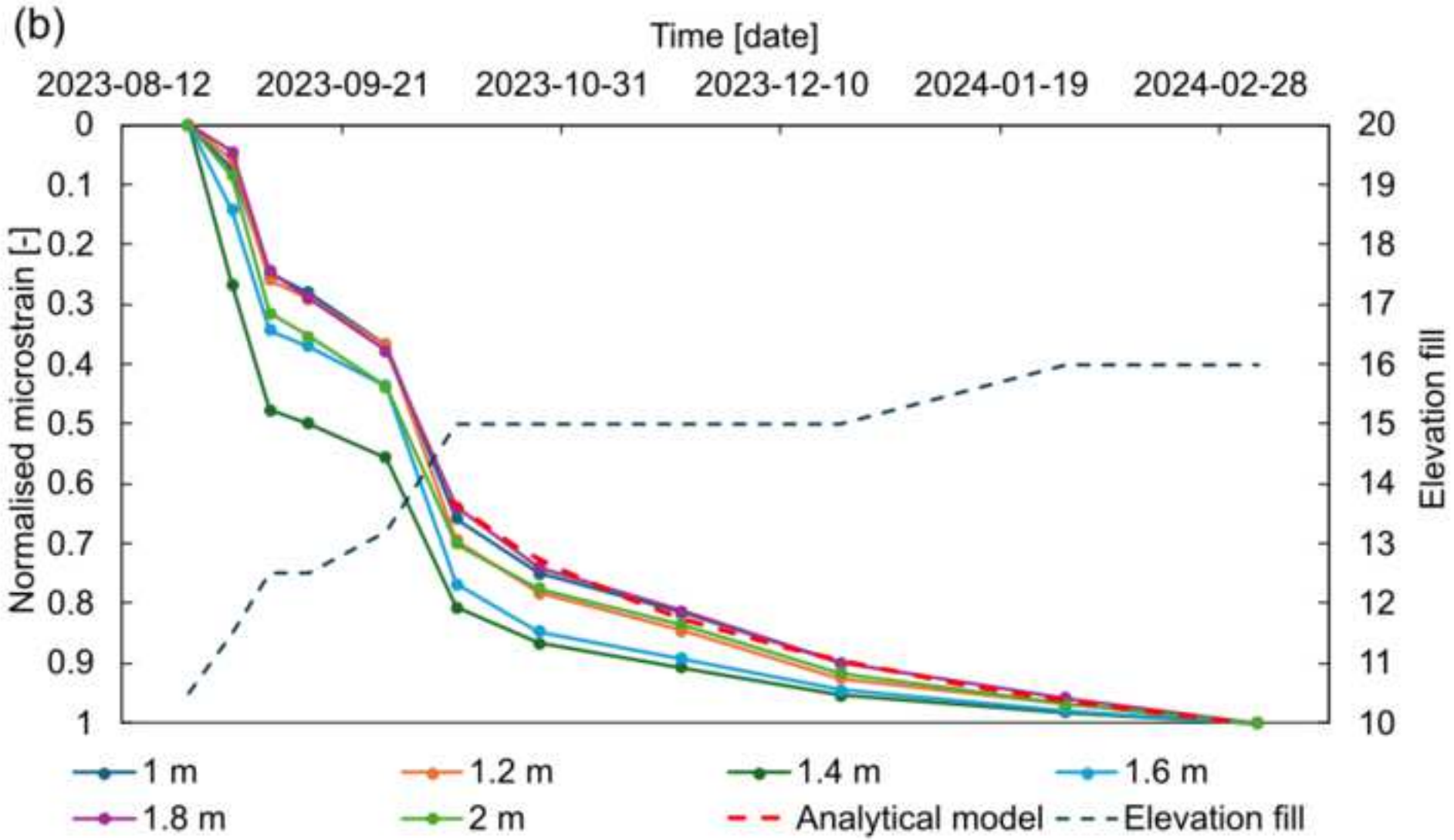

Figure 14a

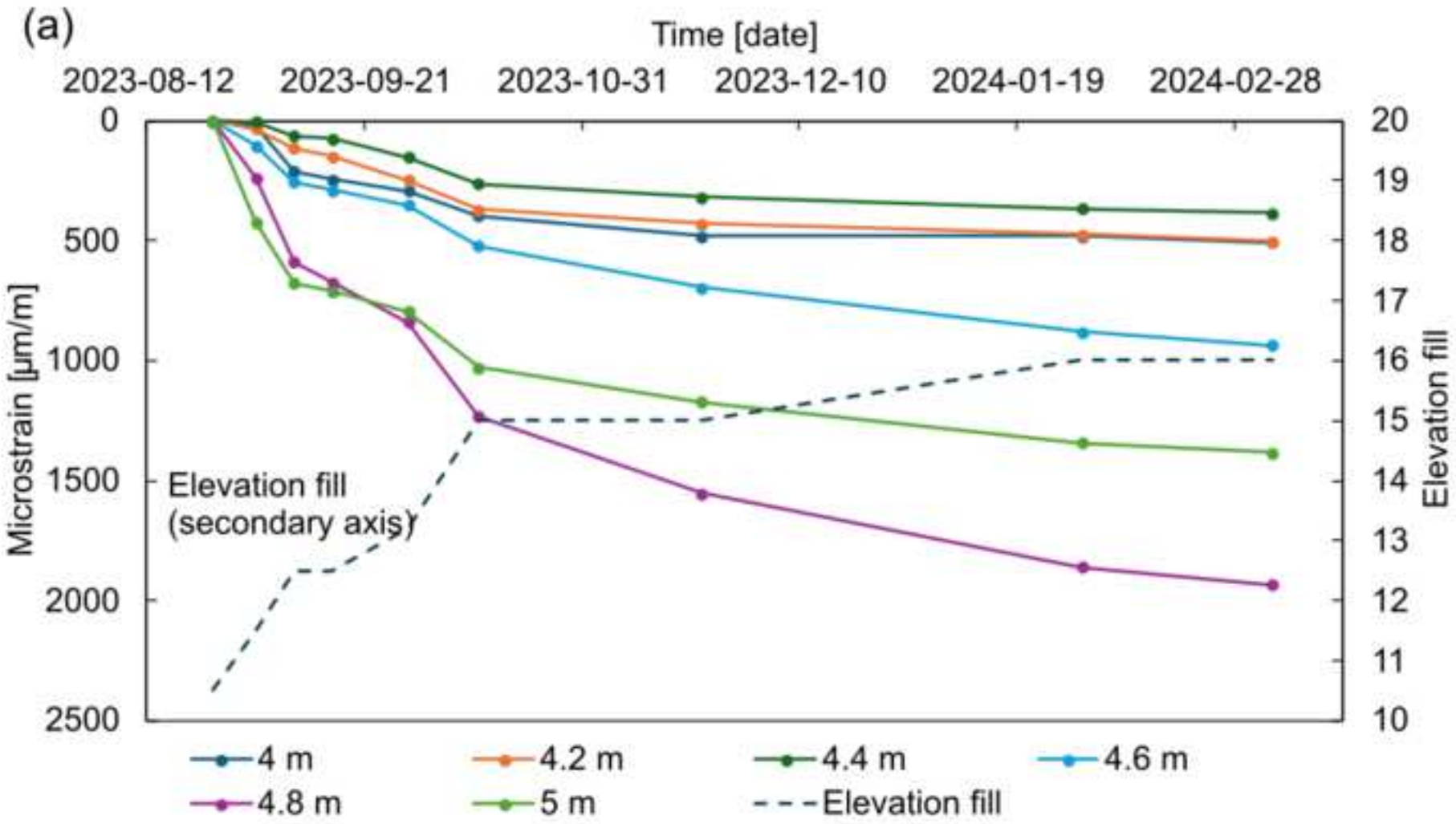

Figure 14b

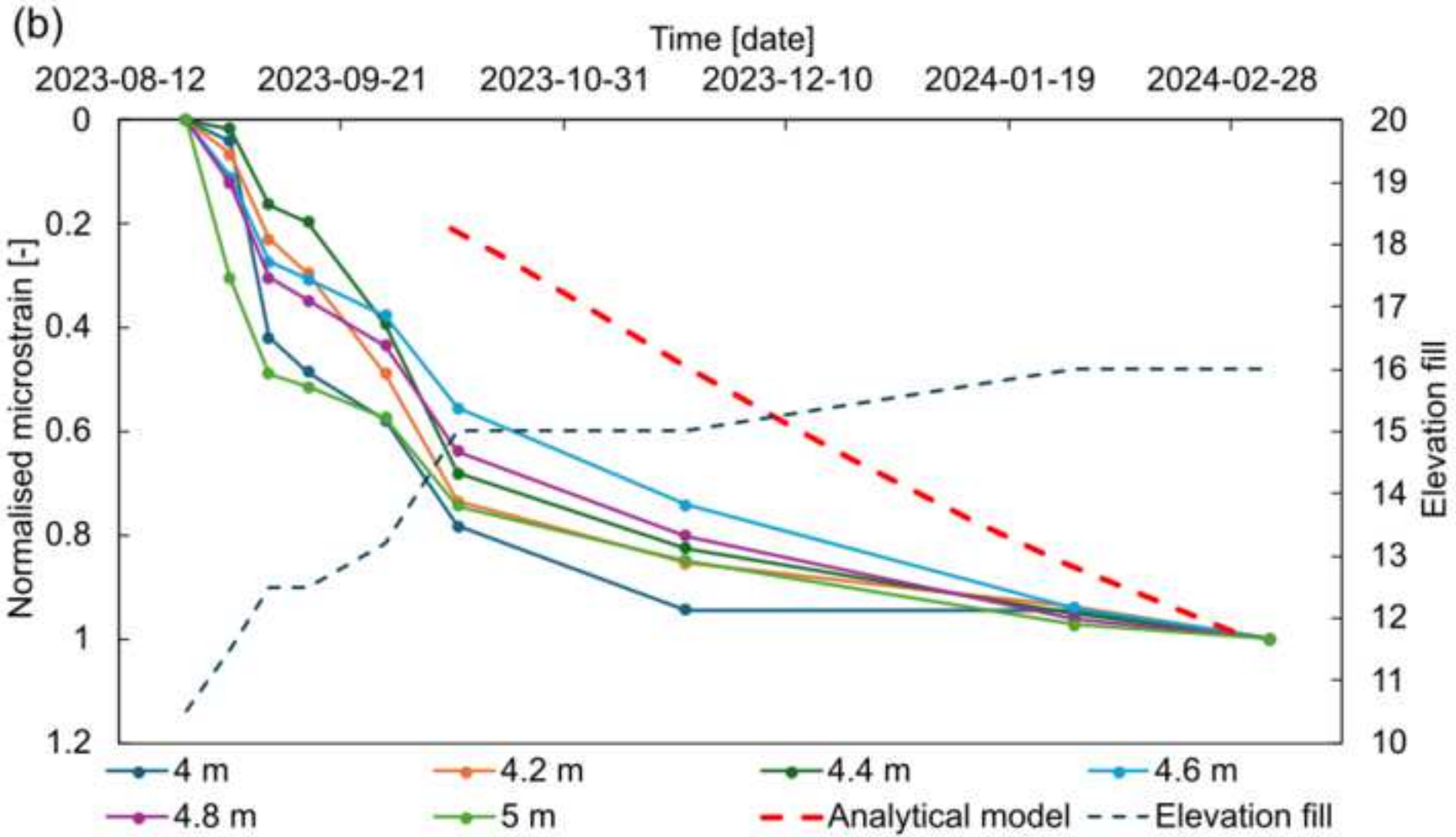

Figure Caption List

Figure 1. Overview of deep mixed columns and instrumentation, (a) plan view, (b) profile view.

Figure 2. Photographs from installation works, a) installation of EpsilonSensors, b) after placement of EpsilonSensors in red protective tubes, c) placement of 3DSensor and settlement plates with risers.

Figure 3. (a) Setup of interrogator OBR4600 and EpsilonSensor in laboratory condition, (b) illustration of optical frequency domain reflectometry (OFDR) using Rayleigh backscattering.

Figure 4. Piezometer data showing temperature in column J5 and natural clay (locations shown in Figure 1).

Figure 5. Piezometer data showing pore pressure in column J5 and natural clay (locations shown in Figure 1). Elevation of fill is shown on the secondary axis.

Figure 6. Vertical displacement of settlement plates and vertical displacement at top of columns L6 and K6 (data from Figure 8). Time period M3 to M10.

Figure 7. Distributed strain sensing data, (a) column L6, (b) column K6.

Figure 8. Vertical displacement, (a) column L6, (b) column K6.

Figure 9. Theoretical considerations of strain coupling between sensor and improved soil. (a) stress equilibrium for a part of the sensor with infinitesimal length dz, (b) schematic illustration of strain profile development over time at slippage.

Figure 10. Mobilised interface shear stress $|\tau_i|$ in column L6, (a) absolute values, (b) degree of mobilised bond strength.

Figure 11. Mobilised interface shear stress $|\tau_i|$ in column K6, (a) absolute values, (b) degree of mobilised bond strength.

Figure 12. Vertically distributed strain data in selected segments of sensor, (a) column L6 between 1.0 m and 2.0 m depth, (b) column K6 between 4.0 m and 5.0 m depth.

Figure 13. Strain over time for 0.2 m increments for column L6 between selected segments (Figure 12), a) strain, b) normalised strain.

Figure 14. Strain over time for 0.2 m increments for column K6 between selected segments (Figure 12), a) strain, b) normalised strain.